# Buoyancy-driven exhumation of lawsonite-bearing eclogites and blueschists in the Lanling area, central Qiangtang Terrane, Tibetan Plateau

Shilin Wang[1], Jinxue Du[2], Zhao Zhongbao[3], Yi Cao[4], Xiao Liang[2], Gen-Hou Wang[5], and Xiaosai Wang[6]

[1]China University of Geosciences (Beijing), School of Earth Science and Resources
[2]China University of Geosciences (Beijing)
[3]Chinese Academy of Geological Sciences
[4]China University of Geosciences (Wuhan)
[5]China University of Geosciences
[6]Institute of Exploration Techniques, Chinese Academy of Geosciences

November 23, 2022

## Abstract

The exhumation mechanism of the low-temperature/high-pressure (LT/HP) rocks, is critical for understanding the formation of the central Qiangtang metamorphic belt (CQMB), Tibetan Plateau, but it is still hotly debated. Here, we report field, petrological, phase-equilibria and petro-physical modelling data on the newly discovered lawsonite-bearing eclogites, epidote eclogite and lawsonite-bearing blueschists from the Lanling area in the CQMB. The mineral characteristics and phase equilibria modeling reveal that the LT/HP rocks record peak P-T conditions from peak pressure ($P_{max}$) of 22.5–23.5 kbar at 460–480 °C to peak temperature ($T_{max}$) of 530–550 °C at 20–22.5 kbar. Combined with previous documented geochronological data, a clockwise P-T-t path for these LT/HP rocks is obtained, which is characterized by pronounced heating decompression (~223–221 Ma), subsequent isothermal decompression (~221–219 Ma), and final cooling decompression (~219–212 Ma). Modeled densities and net buoyancies (defined as the density difference between Preliminary Reference Earth Model and LT/HP rocks) show that all LT/HP samples are buoyant at $P_{max}$, but gradually become denser during heating decompression and evolve to neutrally or negatively buoyant around $T_{max}$. Later mixing with lower-density garnet-phengite schists at $T_{max}$, help the density of the exhuming LT/HP unit reduce to lower than that of the surrounding mantle again during continued isothermal decompression. We concluded that exhumation of eclogites and blueschists is short-lived (~10 Ma) and multi-stage buoyancy-driven characterized by early self-exhumation via diapiric rise and post-$T_{max}$ carried-exhumation along subduction channel.

## Hosted file

`supporting information.docx` available at https://authorea.com/users/546024/articles/602238-buoyancy-driven-exhumation-of-lawsonite-bearing-eclogites-and-blueschists-in-the-lanling-area-central-qiangtang-terrane-tibetan-plateau

# Buoyancy-driven exhumation of lawsonite-bearing eclogites and blueschists in the Lanling area, central Qiangtang Terrane, Tibetan Plateau

**Shilin Wang[1, 2], Jinxue Du[1], Zhongbao Zhao[3, 4], Yi Cao[5], Xiao Liang[1], Genhou Wang[1], Xiaosai Wang[1, 6]**

[1]School of Earth and Resources, China University of Geosciences, Beijing, China
[2]Exploration and Production Research Institute of Northwest Oilfield Company, SINOPEC, Urumqi, China
[3]Key Laboratory of Deep-Earth Dynamics of Ministry of Natural Resources, Institute of Geology, Chinese Academy of Geological Sciences, Beijing, China
[4]Southern Marine Science and Engineering Guangdong Laboratory (Guangzhou), Guangzhou, China
[5]State Key Laboratory of Geological Processes and Mineral Resources, School of Earth Sciences, China University of Geosciences, Wuhan, China
[6]Institute of Exploration Techniques, Chinese Academy of Geosciences, Langfang, Hebei, China

Corresponding author: Jinxue Du (jxdu@cugb.edu.cn); Zhongbao Zhao (zhaozhb04@163.com)

**Key points:**

- Lawsonite-bearing eclogites and lawsonite-bearing blueschists are first discovered in the Lanling area, Central Tibetan Plateau
- PT paths of eclogites and blueschists record $P_{max}$ of 22–23 kbar at 460–480 °C and $T_{max}$ of 530–550 °C at 20–22 kbar
- Exhumation of eclogites and blueschists is proposed to be short-lived and multi-stage buoyancy-driven event

## Abstract

The exhumation mechanism of the low-temperature/high-pressure (LT/HP) rocks, is critical for understanding the formation of the central Qiangtang metamorphic belt (CQMB), Tibetan Plateau, but it is still hotly debated. Here, we report field, petrological, phase-equilibria and petro-physical modelling data on the newly discovered lawsonite-bearing eclogites, epidote eclogite and lawsonite-bearing blueschists from the Lanling area in the CQMB. The mineral characteristics and phase equilibria modeling reveal that the LT/HP rocks record peak P-T conditions from peak pressure ($P_{max}$) of 22.5–23.5 kbar at 460–480 °C to peak temperature ($T_{max}$) of 530–550 °C at 20–22.5 kbar. Combined with previous documented geochronological data, a clockwise P-T-t path for these LT/HP rocks is obtained, which is characterized by pronounced heating decompression (~223–221 Ma), subsequent isothermal decompression (~221–219 Ma), and final cooling decompression (~219–212 Ma). Modeled densities and net buoyancies (defined as the density difference between Preliminary Reference Earth Model and LT/HP rocks) show that all LT/HP samples are buoyant at $P_{max}$, but gradually become denser during heating decompression and evolve to neutrally or negatively buoyant around $T_{max}$. Later mixing with lower-density garnet-phengite schists at $T_{max}$, help the density of the exhuming LT/HP unit reduce to lower than that of the surrounding mantle again during continued isothermal decompression. We concluded that exhumation of eclogites and blueschists is short-lived (~10 Ma) and multi-stage buoyancy-driven characterized by early self-exhumation via diapiric rise and post-$T_{max}$ carried-exhumation along subduction channel.

**Keywords:** lawsonite-bearing eclogite and blueschist, phase equilibria modeling, net buoyancy, exhumation, Qiangtang Terrane, Tibetan Plateau

## 1. Introduction

Eclogites and other (ultra)high-pressure ((U)HP) rocks are formed at pressures above 10 kbar, as indicated by high-pressure minerals such as diamond and coesite (Chopin, 1984; Sobolev & Shatsky, 1990). These high-pressure minerals traditionally indicate that (U)HP rocks can derive from depths of >100 km, well below the usual Moho depth, although some researchers argue that pressure cannot be simply translated to depth owing to the effect of differential stress (see e.g., Reuber et al., 2016; Yamato & Brun, 2017). There is an ongoing controversy on how (U)HP rocks, especially eclogites, can be brought to the surface (Hacker & Gerya, 2013; Platt, 1993; Warren, 2013). A range of models have been proposed to account for the exhumation of eclogites, and they can be grouped in two classes: buoyancy-driven exhumation and external tectonic force induced exhumation.

The buoyancy-driven exhumation model for continental-type (U)HP eclogites is well accepted, as the subducted continental crust is believed to have lower density compared to the surrounding mantle (e.g., Davies & von Blanckenburg, 1995; Ernst, 2001; Ernst et al., 1997). For oceanic-type (U)HP eclogites, however, it is hotly debated whether they can exhume autonomously or has to be driven by external forces. Experimental studies demonstrate that mid-ocean ridge basaltic (MORB) eclogites have densities greater than the surrounding mantle above the depths of the core-mantle boundary (Aoki & Takahashi, 2004; Irifune et al., 1986; Ricolleau et al., 2010). Therefore, oceanic eclogites cannot exhume by their own negative buoyancies, but the external buoyancies from low-density metasediments (Platt, 1986), serpentinites (Hermann et al., 2000), and subducted continental crust (Ernst, 2001), and/or the external tectonic forces, such as corner flow (Shreve & Cloos, 1986) and plunger expulsion (Warren et al., 2008) are needed. To better understand the exhumation mechanisms, change of the densities of subducted eclogites along their pressure-temperature (P-T) paths during subduction and exhumation processes have to be constrained.

Based on phase equilibria modeling and density calculations, Agard et al. (2009) and Chen et al. (2013) demonstrate that peak P-T conditions of all natural oceanic (U)HP eclogites, except for few exceptions from Alpine Zermatt-Saas and the Monviso and Voltri massifs, lie in the positive net buoyancy (defined as $\Delta\rho=\rho_{mantle}-\rho_{protolith}$) field of representative MORB compositions. Wang et al. (2019)

divide the exhumed oceanic eclogites into two categories based on the modeled density of a MORB composition: the self-exhumation type ($\Delta\rho>0$, all lawsonite eclogites) and the carried-exhumation type ($\Delta\rho<0$, nearly all epidote eclogites). Furthermore, Wang et al. (2019) proposed that retrograde metamorphism affects the densities of eclogites, and thus their exhumation, e.g., following heating decompression P-T path, exhumation of oceanic eclogites would be obstructed due to dehydration-induced density increase. However, the densities and net buoyancies of natural oceanic eclogites, especially their variations along decompression P-T paths, may be more important for understanding the exhumation of subducted oceanic crusts compared to the estimations using the compositions of average oceanic crust or MORB (Agard et al., 2009; Chen et al., 2013; Wang et al., 2019).

Eclogites (e.g. Li et al., 2006; Zhai et al., 2009a; 2011a; Zhang et al., 2006a), lawsonite-bearing blueschists (Liang et al., 2017; Liu et al., 2011; Lu et al., 2006; Tang & Zhang, 2014) and lawsonite-bearing phengite schists (Wang et al., 2018) have been reported in the central Qiangtang metamorphic belt (CQMB), Tibetan Plateau. Peak *P-T* conditions of these low-temperature/high-pressure (LT/HP) rocks reveal that they may have experienced lawsonite eclogite facies metamorphism (Wang et al., 2018; Zhai et al., 2009a; 2011a), though lawsonite-bearing eclogites have never been found in the CQMB. Moreover, exhumation mechanisms of the LT/HP rocks in the CQMB are still highly debated. Kapp et al. (2000; 2003; 2019) and Pullen and Kapp (2014) insist that the high-pressure mélange derived from southward subduction of the Jinsha suture and was exhumed by domal low angle normal faulting. This dome exhumation model, however, is denied by the results of 3D modeling that show large-scale compression thrust structure in the CQMB and by the observations that mélange lies both above and below LT/HP sheet rather than only above in the CQMB (Zhao et al, 2014; 2015). The *in-situ* northward oceanic subduction model explains the exhumation of HP rocks as the result of slab break-off followed by overthrusting onto the south Qiangtang Terrane (SQT; Li et al., 2009; 2015; Zhao et al., 2014) or extrusion followed by large-scale detachment faulting (Liang et al., 2017). Zhao et al. (2015) and Li et al. (2020) proposed a divergent double subduction model, which suggests that high-pressure rocks were derived from the short and south-dipping slab of the Paleo-Tethys Ocean and exhumed by extraction beneath the SQT followed by thrusting on top of the ophiolitic mélange. These exhumation models are proposed based primarily on structural observations, but the metamorphic evolution and density variation of high-pressure rocks and their effects on exhumation process have not been fully addressed.

In this paper, we report newly discovered lawsonite-bearing eclogites (law-EC), epidote eclogite (ep-EC) and lawsonite-bearing blueschists (law-BS) from the Lanling area in the CQMB, central Tibetan Plateau. Based on the comprehensive petrography, mineral chemistry and phase equilibria modelling analyses on these rocks, density and net buoyancy evolution of the LT/HP rocks during the closure of the Paleo-Tethys ocean are constrained. These results may resolve some ambiguities about exhumation process in the CQMB, as well as provide insights into the exhumation mechanism of the subducted oceanic crust in general.

## 2. Geological setting

Located in the central Tibetan Plateau, Qiangtang Terrane is separated from the Songpan-Ganze terrane by the Jinsha suture to the north and from the Lhasa terrane by the Bangong-Nujiang suture to the south (Fig. 1; Yin & Harrison, 2000). It can be divided into the north Qiangtang Terrane (NQT) and the south Qiangtang Terrane (SQT) by the central Qiangtang metamorphic belt (Zhang et al., 2006b; Zhao et al., 2015). The SQT is occupied by unmetamorphosed or sub-greenschist facies marine deposits aged from the Carboniferous to the Jurassic (e.g., Hu et al., 2015; Li et al., 2018), whereas the NQT is covered by Cambrian-Jurassic marine strata and records episodes of arc-related magmas that formed during subduction and break-off of Paleo-Tethys oceanic slab (Jiang et al., 2015; Zhai et al., 2011b). The CQMB, remnants of the Paleo-Tethys oceanic subduction (e.g., Liang et al., 2012; 2017; Liu et al., 2011; Zhai et al., 2011b; Zhao et al., 2014; 2015), is exposed as thrust sheets within Carboniferous-Permian strata (e.g., Zhao et al., 2015).

Generally, the CQMB exhibits a mélange structure that is characterized by chaotic juxtaposition of weakly deformed meter-to-kilometer-sized eclogite, blueschist, and amphibolite facies blocks within a strongly deformed but weakly metamorphosed sedimentary matrix (e.g., Kapp et al., 2003; Zhao et al., 2015). Eclogites and blueschists display enriched mid-ocean ridge basalt (E-MORB), normal mid-ocean ridge basalt (N-MORB) or ocean island basalt (OIB) affinities (Tang & Zhang, 2014; Zhai et al., 2011b; Zhang et al., 2010; 2014). The LT/HP rocks were formed and exhumed mainly during the Late Triassic, which was supported by garnet-clinopyroxene-whole-rock Lu-Hf ages of 244–223 Ma (Pullen et al., 2008), zircon U-Pb ages of 230±4 and 237±4 Ma (Zhai et al., 2011a) and $^{40}Ar$-$^{39}Ar$ ages of 227–202 Ma (Kapp et al., 2003; Liang et al., 2012; Zhai et al., 2009b; 2011a). Therefore, these LT/HP rocks represent the remnant of the closing Paleo-Tethys Ocean (e.g., Li et al., 2006; Liang et al., 2012; Zhai et al., 2011a, b).

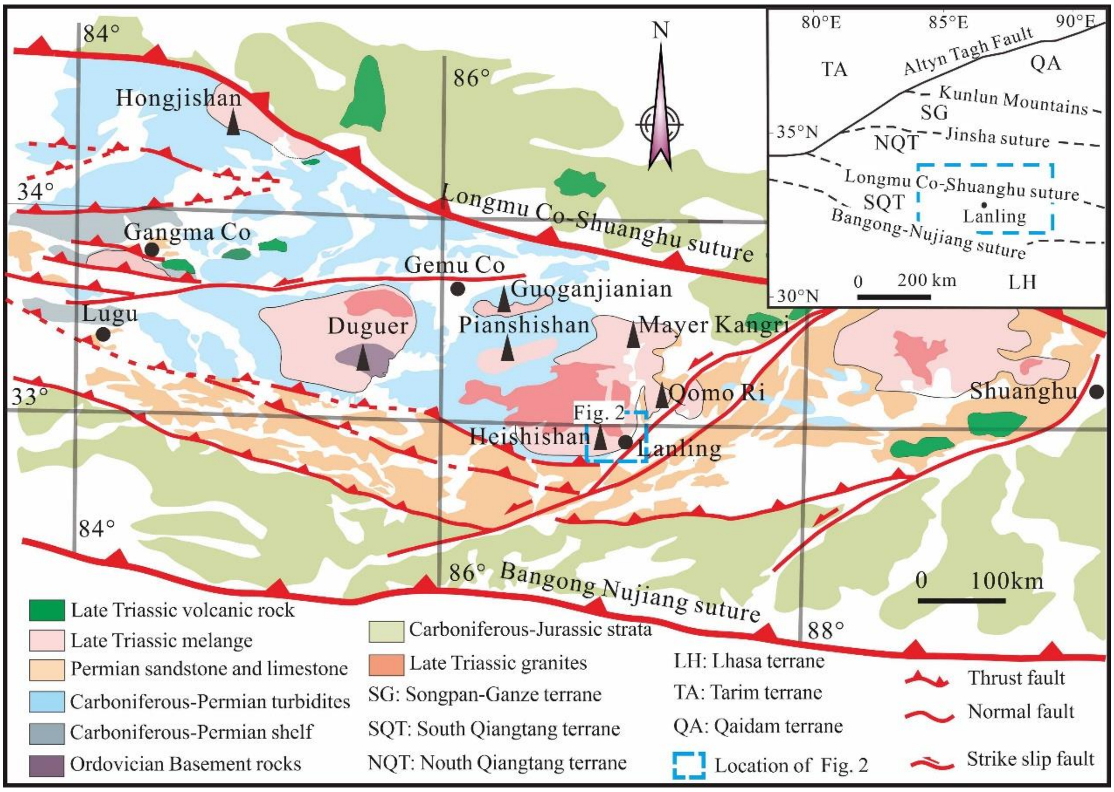


Fig. 1. Simplified geological map of the Central Qiangtang metamorphic belt (CQMB) modified after Li et al. (2018). The inset shows the location of the CQMB in the Tibet Plateau.

The newly discovered law-EC, ep-EC and law-BS were sampled from the core domain of the Lanling metamorphic block within the CQMB (Figs. 1 and 2). The main unit of the N-S striking Lanling metamorphic block includes, from bottom to top, greenschist-facies Precambrian basements, Carboniferous sediments with extensive folding and cleavages, ophiolitic mélange, and strongly deformed subduction sedimentary mélange that encloses large bodies of LT/HP rocks and Permian limestone (Zhao et al., 2014; 2015). Along the transversal direction (Fig. 2), rocks of different metamorphic grades are symmetrically distributed, with garnet blueschists (i.e., lawsonite-bearing blueschists in this study, the same as below) in the core domain, epidote blueschists in the mantle domain, and greenschists in the margin domain (Liang et al., 2017). All LT/HP rocks are unconformably overlain by the unmetamorphosed

Late Triassic accretionary complex (Liang et al., 2012; Zhao et al., 2014). From outcrop view, blueschists and eclogites unexceptionally occur as diameters-to-meters-sized lenses in the foliated garnet-phengite schists (i.e., lawsonite-bearing phengite schists in Wang et al. (2018), the same as below) and subordinate marble (Fig. 3; Liang et al., 2017).

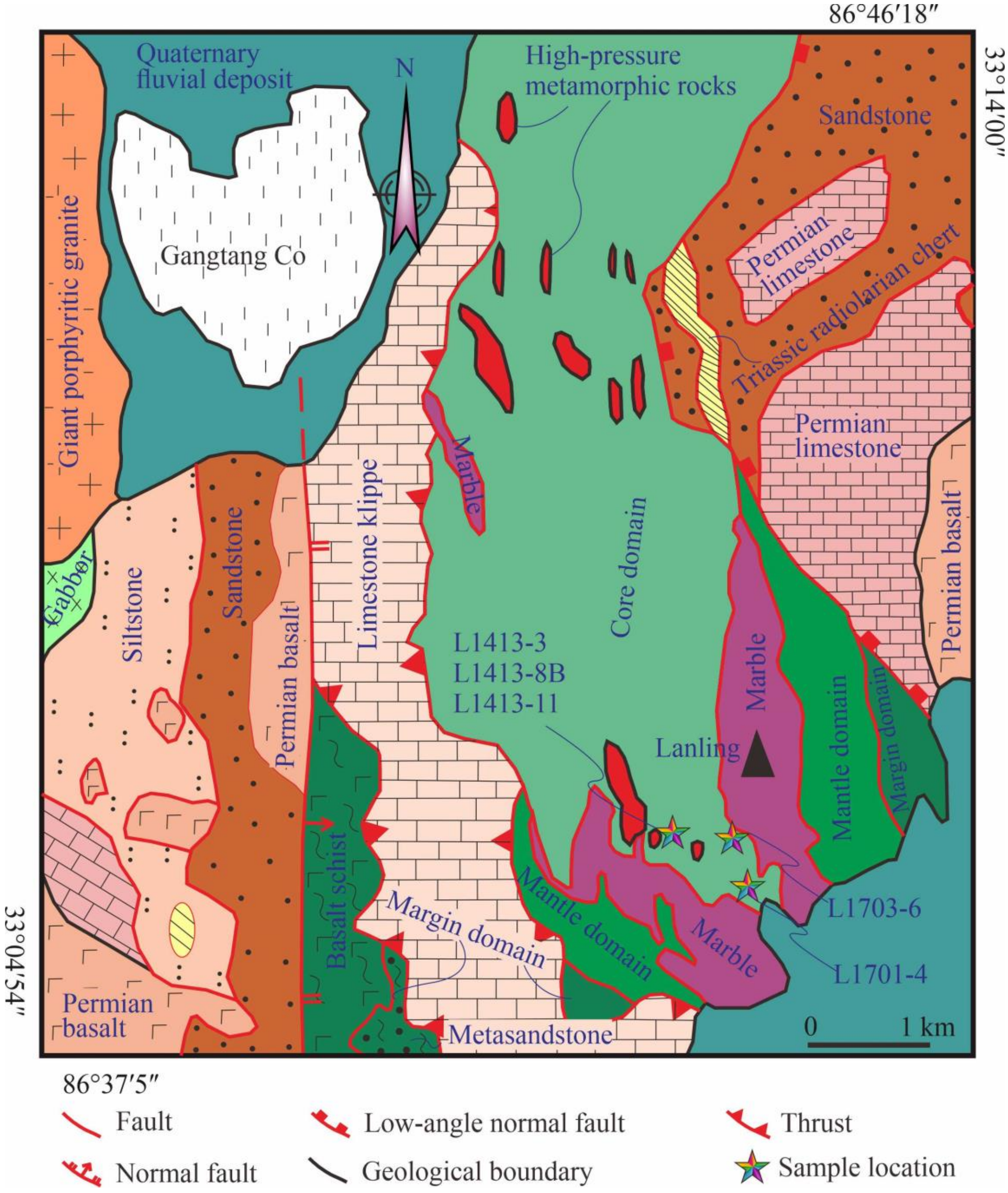


Fig. 2. Sketching geological map of the symmetric Lanling metamorphic belt modified after Liang et al. (2017)

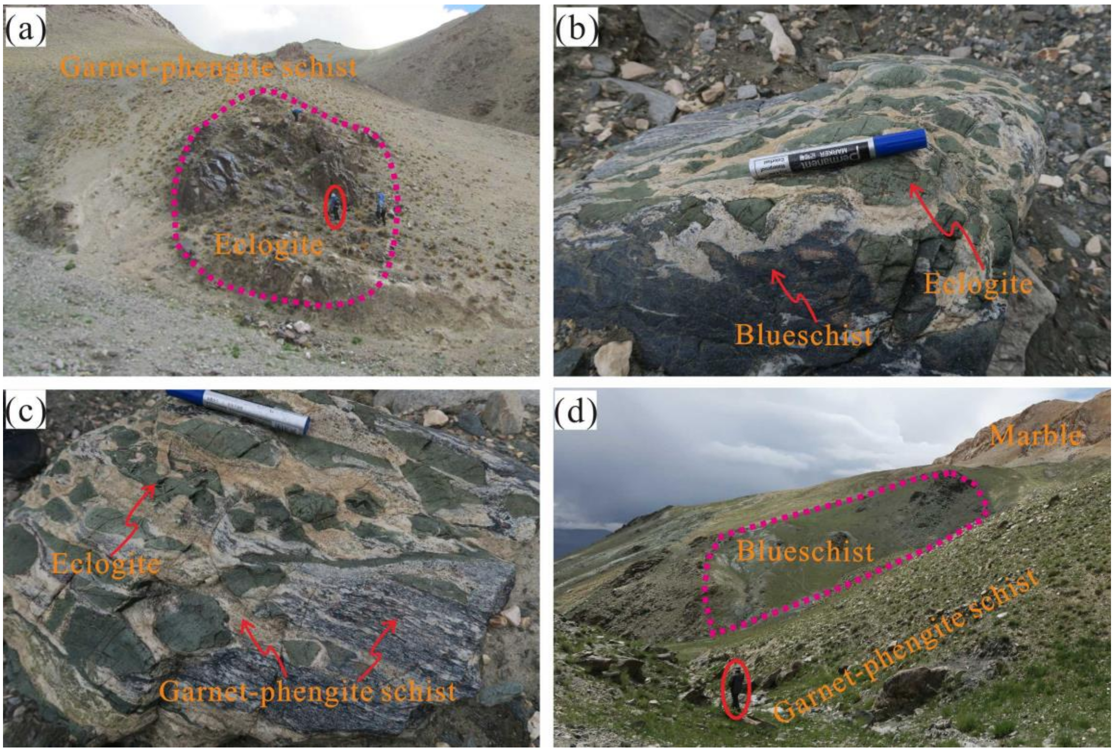


**Fig. 3.** Field photographs of eclogites, blueschists, and garnet-phengite schists from the Lanling area, Qiangtang terrane, central Tibetan Plateau.

## 3. Analytical methods

### 3.1. Whole-rock X-Ray Florescence analysis

Whole-rock major elements are determined using an Axios$^{max}$ X-ray fluorescence (XRF) spectrometer at the institute of Regional Geological Survey of the Hebei Province. The loss on ignition (LOI) is determined by P124S electronic analytical balance. FeO content is obtained via $Fe^{2+}$ titration and the $Fe_2O_3$ content is calculated by the difference between $FeO^{total}$ and FeO. The relative analytical uncertainties for major elements are less than 5%.

### 3.2. Mineral microprobe analysis

To analyze mineral compositions, electron microprobe analyses (EMPA) are performed on JXA-8230 at the Institute of Regional Geological Survey of the Hebei Province and at the Key Laboratory of Mineral Resources Evaluation in Northeast Asia, Ministry of Land and Resources, College of Earth Sciences, Jilin University. The main operation conditions of EMPA are 15 kV accelerating voltage, 10 nA beam current, 10 s counting time and 2 μm beam diameter (5 μm for paragonite). The PRZ correction is performed to convert raw intensities to oxide wt. % utilizing SPI 53 minerals standard (U.S.). The relative analytical uncertainties are <2% for major elements. The representative analytical data are presented in Tables 1–3.

### 3.3. Phase equilibria modeling

Phase equilibria modeling was performed for all studied samples using Theriak-Domino software (de Capitani & Petrakakis, 2010) and the updated internally consistent thermodynamic dataset (Holland & Powell, 1998). A series of P-T pseudosections were constructed in the model systems MnO-$Na_2O$-CaO-FeO-MgO-$Al_2O_3$-$SiO_2$-$H_2O$-$Fe_2O_3$ (MnNCFMASHO) for the ep-EC sample L1701-4 and MnO-$Na_2O$-CaO-$K_2O$-FeO-MgO-$Al_2O_3$-$SiO_2$-$H_2O$-$Fe_2O_3$ (MnNCKFMASHO) for the other samples. The fluid phase was assumed to be pure $H_2O$ and in excess due to the presence of a great amount of hydrous minerals (e.g., lawsonite, epidote/zoisite, phengite and glaucophane). The mineral A-X models are biotite and garnet (White et al., 2005); chlorite, epidote and talc (Holland & Powell, 1998); clinoamphibole (Diener et al., 2007); feldspar (Baldwin et al., 2005; Holland & Powell, 2003); omphacite (Green et al., 2007); and white mica (Coggon & Holland, 2002). Pure end-member phases include albite, coesite/quartz, $H_2O$, kyanite and lawsonite. Abbreviations for minerals and end-members follow the notations given by Holland & Powell (1998). Furthermore, *Sensu lato* names of glaucophane, hornblende (involving barroisite, winchite and magnesio-hornblende) and actinolite (Dale et al., 2005) were adopted to distinguish amphibole group minerals.

### 3.4. The effective whole-rock compositions used for phase equilibria modeling

Considering element fractionation caused by growth of porphyroblasts (e.g., zoned garnet) during prograde metamorphism (Marmo et al., 2002), effective bulk-rock compositions were calculated by integrating the modal proportions of minerals and their representative EPMA compositions (Carson et al., 1999). For samples L1701-4, L1413-3, L1413-8B and L1703-6, the original unfractionated effective bulk-rock compositions were used. These compositions are based on the modal abundances of all relevant phases and are suggested to be valid to model the growth of garnet core (Du et al., 2014a). On the contrary, the fractionated effective bulk-rock compositions, which are valid for modeling garnet rim, only take into account half the mode of the chemically zoned phases (e.g., garnet) and their rim compositions (Table 4). This approach has been successfully employed to estimate peak P-T conditions of eclogites and blueschists (Du et al., 2014a; Scodina et al., 2019; Wei et al., 2010). As to sample L1413-11, which suffered stronger retrograde metamorphism than the other samples, it is challenging to obtain an effective bulk-rock composition. Alternatively, the compositions of garnet from this sample were simply plotted on the P-T pseudosections constructed using the sample L1413-3. This indirect method has been proved valid to estimate P-T conditions of low-temperature eclogites with similar bulk-rock compositions (Du et al., 2014b; Wei & Clarke, 2011).

### 3.5. The density calculations

The densities of law-EC, ep-EC, law-BS, and law-PS (lawsonite-bearing phengite schist) were calculated using Theriak-Domino software in the model system of MnO-$Na_2O$-CaO-$K_2O$-FeO-MgO-$Al_2O_3$-$SiO_2$-$H_2O$-$TiO_2$-$Fe_2O_3$ (MnNCKFMASHTO) in the P-T range of 25–600 °C and 0–30 kbar. The XRF compositions of law-EC sample L1413-3, ep-EC sample L1701-4, law-BS sample L1414-1 and law-PS sample L1414-7 (the latter two are taken from Wang et al. (2018)) are used for density calculation. The net buoyancy is defined as the density difference between the Preliminary Reference Earth Model (PREM; Fig. S1; Dziewonski & Anderson, 1981) and the studied LT/HP rocks at giving P-T conditions, namely $\Delta\rho=\rho_{PREM}-\rho_{LT/HP}$.

## 4. Petrography

According to the mineral assemblages and the volume proportions of the major phases, our studied samples are divided into law-EC (e.g., samples L1413-3 and L1413-11), ep-EC (e.g., sample L1701-4) and law-BS (e.g., sample L1413-8B and L1703-6). All samples are generally porphyroblastic, massive or weakly foliated.

### 4.1. Ep-EC

Sample L1701-4 displays a medium- to fine-grained porphyroblastic texture and consists of garnet (2%; vol. %, the same below), omphacite (30%), epidote/allanite (40%), glaucophane (5%), hornblende/actinolite (15%), albite (3%) and quartz (1%), with minor rutile, ilmenite, sphene and chlorite (Fig. 4a). Garnet occurs as hypidioblastic to idioblastic porphyroblasts (0.4–1.2 mm in diameter) and shows inclusion-rich core overgrown by relatively cleaner rim (Fig. 4a, b). Garnet is commonly overprinted by xenoblastic chlorite, albite and actinolite along grain boundaries and cracks (Fig. 4b). Inclusions in the garnet are primarily omphacite, glaucophane and rare quartz (Fig. 4b), and secondarily epidote and hornblende (overgrowing on glaucophane). Both omphacite and glaucophane occur either as fine-grained hypidioblastic to idioblastic crystals (0.1–0.3 mm in size) in the matrix (Fig. 4a, b, c) or as inclusions (<0.1 mm in size) in the porphyroblastic garnet and epidote (Fig. 4b, d). They are usually overgrown by hornblende and albite, and occasionally by actinolite (Fig. 4c). Epidote occurs as inclusions (mostly ~0.2 mm in size) in the garnet (Fig. 4b) or as porphyroblasts (0.2–0.5 mm in size) in the matrix (Fig. 4a, b and d). Epidote in the matrix contains numerous inclusions of omphacite and sphene and occasionally shows allanite cores (Fig. 4d). Albite, occasionally coexisting with chlorite, occurs along the cracks of garnet or in the pressure shadow of garnet, omphacite or glaucophane (Fig. 4b, c).

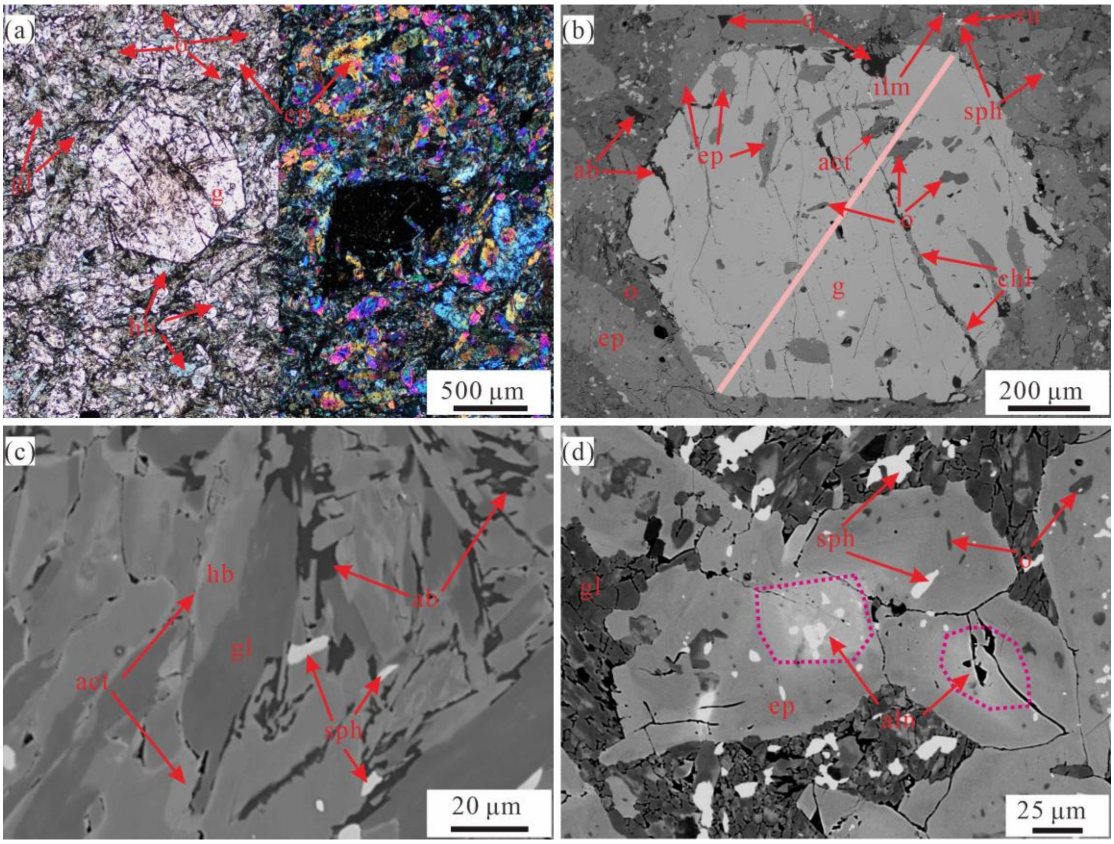


Fig. 4. Photomicrographs and backscattered electron (BSE) images showing textural relationships in the epidote eclogite L1701-4. (a) Idioblastic to hypidioblastic garnet porphyroblasts with omphacite, glaucophane and epidote in the matrix. (b) An idioblastic garnet porphyroblast with primary inclusions of omphacite and secondary inclusions of epidote and actinolite, as well as chlorite and albite within the cracks. (c) Glaucophane partially replaced by albite and hornblende with an outmost rim of actinolite. (d) Idioblastic epidote porphyroblasts with allanite cores showing inclusions of omphacite and sphene. The pink line across garnet shows the location of

the zoning profile in Fig. 7a.

### 4.2. Law-EC

The lawsonite-bearing eclogite samples L1413-3 and L1413-11 also display a fine-grained porphyroblastic texture and experienced strongly retrograde overprinting with only a few lawsonite and omphacite relicts enclosed in the porphyroblastic garnet or remaining in the matrix (Fig. 5).

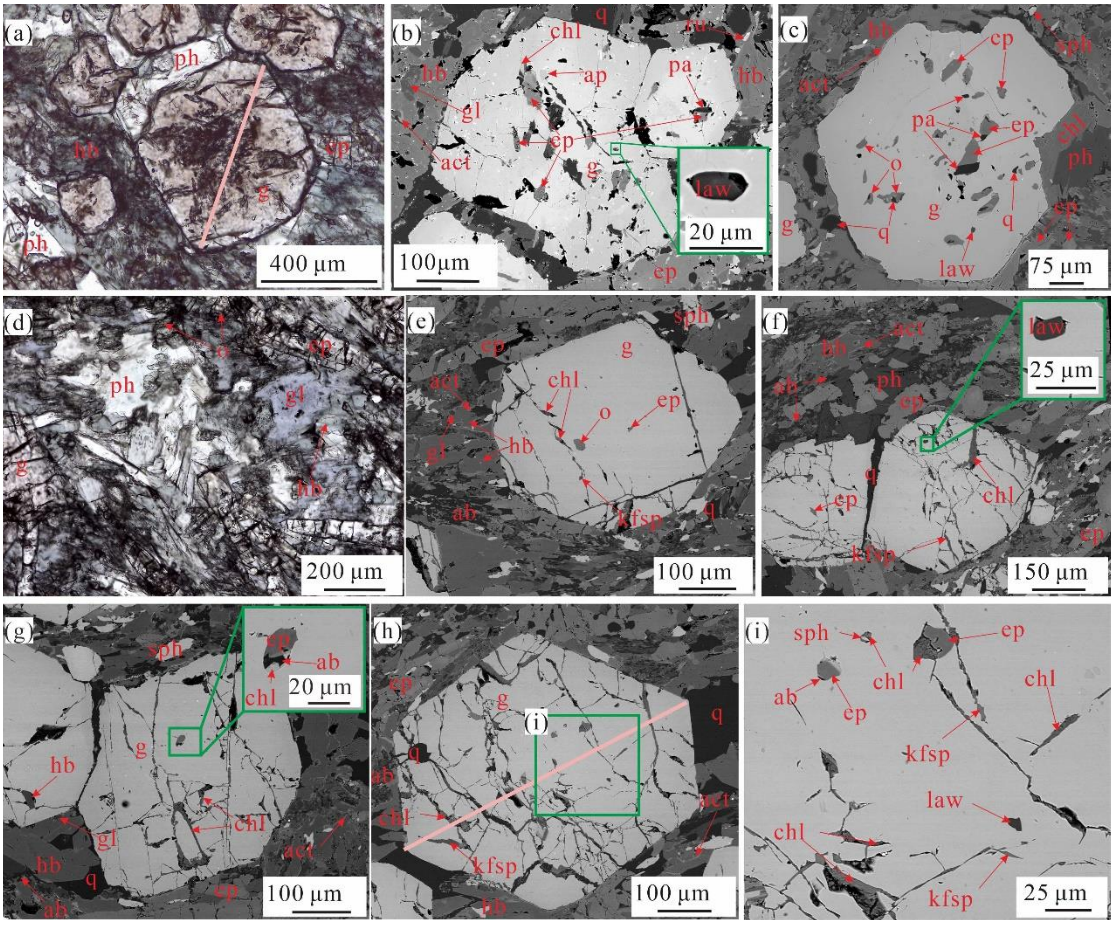


Fig. 5. Photomicrographs and backscattered electron images showing textural relationships in the lawsonite-bearing eclogites L1413-3 and L1413-11. (a) Hypidioblastic garnet porphyroblasts with epidote and hornblende in the matrix and phengite in the pressure shadow in Law-EC L1413-3. (b-c) Idioblastic to hypidioblastic garnet porphyroblasts with primary inclusions of lawsonite, omphacite and rare quartz and secondary inclusions of epidote, paragonite, and aggregates of epidote + paragonite and epidote + albite, as well as chlorite and albite within cracks in Law-EC L1413-3. (d) Matrix omphacite coexisting with glaucophane, epidote and phengite in Law-EC L1413-3. (e) and (f) hypidioblastic garnet porphyroblasts with inclusions of omphacite and lawsonite in a matrix of gl/hb + ph + ep + q in Law-EC L1413-11. (g–i) Idioblastic to hypidioblastic garnet porphyroblasts with primary inclusions of lawsonite and secondary inclusions of epidote, hornblende, and aggregates of epidote ± albite ± chlorite and chlorite +

sphene, as well as chlorite, k-feldspar and albite within the cracks in Law-EC L1413-11. The orange lines across garnet crystals in (a) and (h) show the location of the zoning profiles Fig. 7b and 7c respectively.

Sample L1413-3 consists of garnet (20%), omphacite (2%), glaucophane (3%), epidote (6%), phengite (3%), hornblende/actinolite (50%), albite (5%) and quartz (3%), with minor lawsonite, paragonite, chlorite, rutile, ilmenite and sphene. Garnet, as fine-grained idioblastic porphyroblasts (0.3–0.7 mm in diameter), is obviously zoned with an inclusion-rich core overgrown by a cleaner rim (Fig. 5a–c). It contains the primary inclusions of omphacite (0.01–0.04 mm in size), lawsonite (~0.01 mm in size) and rarely quartz, and secondary inclusions of box-shaped epidote + paragonite ± chlorite or epidote + albite aggregates (Fig. 5b, c). Chlorite, occasionally coexisting with albite, fills the cracks in garnet (Fig. 5b). Omphacite in the matrix occurs as xenoblastic crystals (0.1–0.2 mm in size) and is commonly overgrown by hornblende and albite (Fig. 5e, d). Glaucophane occurs as fine-grained porphyroblasts (0.1–0.2 mm in size) and is often overgrown by hornblende in the mantle and by actinolite in the outermost rim (Fig. 5b, d). Phengite flakes in the matrix are fine-grained (0.1–0.4 mm in size) and usually occur as aggregates around garnet or omphacite (Fig. 5a, d). Hornblende and actinolite, commonly with albite, exist at the rim of glaucophane or as idioblastic porphyroblasts (0.05–0.1 mm in size) in the matrix (Fig. 5a–d).

Sample L1413-11 is mainly composed of garnet (15%), epidote (5%), phengite (2%), hornblende/actinolite (60%), albite (10%) and quartz (2%), with minor omphacite, glaucophane, lawsonite, chlorite, rutile, ilmenite and sphene (Fig. 5e–i). In sample L1413-11, hornblende/actinolite and albite show higher abundances than sample L1413-3 and occur as retrograde products around glaucophane in the matrix (Fig. 5e, f). Fine-grained omphacite and lawsonite (~0.01 mm in size) are only preserved in the porphyroblastic garnet (Fig. 5e). Apart from epidote + albite, aggregates of epidote + albite + chlorite, epidote + chlorite and sphene + chlorite also occur as inclusions in the garnet (Fig. 5g–i). Similar to sample L1413-3, cracks in the garnet are also filled with fine-grained xenoblastic chlorite flakes, albite, and occasionally K-feldspar (Fig. 5e–i).

### 4.3. Law-BS

Both lawsonite-bearing blueschist samples L1413-8B and L1703-6 display a medium- to fine-grained porphyroblastic texture, in which lawsonite occurs only as inclusions in the porphyroblastic garnet (Fig. 6).

Sample L1413-8B consists of garnet (6%), glaucophane (75%), epidote (10%), hornblende (2%), albite (3%), phengite (1%) and quartz (1%), with minor lawsonite, paragonite, chlorite, rutile, ilmenite and sphene (Fig. 6a–c). Garnet occurs as medium-grained porphyroblasts (0.8–1.8 mm in diameter) and shows similar zoning to that of eclogitic samples, with inclusion-rich cores and inclusion-poor rims (Fig. 6a, c). Garnet contains primary inclusions of glaucophane, lawsonite, rutile and rare quartz, and secondary inclusions of epidote and paragonite monophase, and aggregates of epidote + paragonite ± chlorite and chlorite + albite (Fig. 6a–c). Garnet is commonly corroded with its rims partially or completely replaced by chlorite ± albite (Fig. 6a, c). Glaucophane occurs as fine-grained inclusions (< 0.01 mm) within the garnet, rutile and epidote (Fig. 6a–c), or as hypidioblastic to idioblastic grains occasionally with rims of hornblende in the matrix (Fig. 6c). Matrix phengite flakes often occur as hypidioblastic to idioblastic porphyroblasts in the pressure shadows of garnet (Fig. 6c). Hornblende appears as rims of glaucophane occasionally with albite or as xenoblastic porphyroblasts (< 0.01 mm in size) in the matrix (Fig. 6c).

Sample L1703-6 contains garnet (12%), glaucophane (65%), epidote (15%), hornblende (1%), albite (1%), phengite (1%) and quartz (1%), with minor lawsonite (Fig. 6d), rutile, sphene and paragonite (Fig. 6d–f). Garnet in this sample contains not only inclusions of glaucophane, lawsonite, rutile and quartz, similar to sample L1413-8B, but also monophase inclusions of paragonite, epidote, hornblende, albite and calcite, in the vicinities of intra-garnet cracks (Fig. 6d–f).

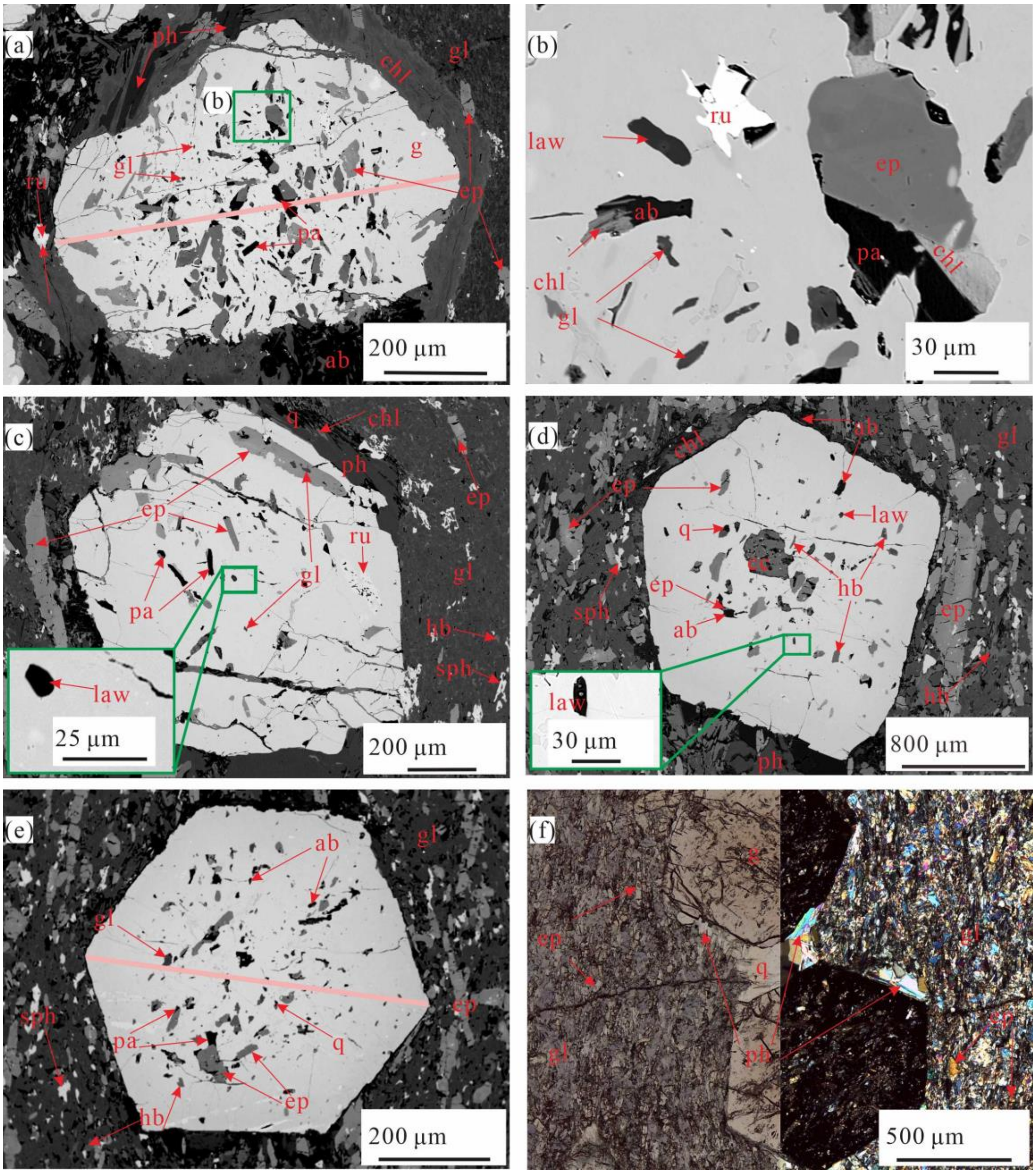


Fig. 6. Photomicrographs and backscattered electron images showing textural relationships in the lawsonite-bearing blueschists L1413-8B and L1703-6. (a–c) Hypidioblastic garnet porphyroblasts with primary inclusions of lawsonite, rutile and glaucophane, and secondary inclusions of epidote, paragonite, sphene and ilmenite and aggregates of epidote + paragonite ± chlorite and chlorite + albite in Law-BS L1413-8B. (d) and (f) Idioblastic garnet porphyroblasts with primary inclusions of lawsonite, glaucophane and rare quartz, and secondary inclusions of epidote, hornblende, calcite and aggregates of epidote + paragonite and epidote + albite in Law-BS L1703-6. (f) Hypidioblastic to idioblastic phengite flakes and quartz in pressure shadows of garnet in Law-BS L1703-6. The orange lines across garnet crystals in (a) and (h) show the location of the zoning profiles in Fig. 7d and 7e respectively.

## 5. Mineral chemistry

### 5.1. Garnet

Garnets in all ep-EC, law-EC and law-BS samples exhibit resembling Mn and Mg profiles with a bell-shaped pattern, which decrease in the spessartine content [=Mn/(Mg + Mn + Ca + $Fe^{2+}$)×100] and gradually increase in the pyrope content [=Mg/(Mg + Mn + Ca + $Fe^{2+}$)×100] from core to rim (Fig. 7a–e). The outmost rims have the lowest spessartine contents (1.0–2.1 mol.%) and highest pyrope contents (9.7–12.6 mol.%; Tables 1–3; Fig. 7a–e), indicating well-developed growth zonings (Spear, 1993). The grossular contents [=Ca/(Mg + Mn + Ca + $Fe^{2+}$)×100] of garnets in all samples, except for law-EC L1413-3, remain almost constant or increase subtly rim-ward (mainly in the range of 22.9–31.1 mol.%). These core-to-rim variations of the spessartine, pyrope and grossular contents of garnets are very similar to those in the garnet blueschists from the same area previously reported by Liu et al. (2011). Garnet in law-EC L1413-3, however, is different from the other four samples, by displaying an obvious two-stage composition zoning with a sharp transition between core and rim (Fig. 7b): the core is almost compositionally constant ($alm_{47.9–62.0}gr_{26.2–37.3}py_{1.3–2.4}spss_{9.3–17.9}$; alm=Ca/(Mg + Mn + Ca + $Fe^{2+}$)×100), while the rim shows a rim-ward gradual increase of the grossular content (26.0 → 33.7 mol.%) and a gradual decrease of the almandine content (66.8 → 55.8 mol.%). The almandine contents of garnets in the law-EC sample L1413-11 and the law-BS sample L1703-6 present similar rim-ward trends as the law-EC sample L1413-3, except for a smooth transition between core and rim (Fig. 7c, e). The almandine content of garnet in the ep-EC sample L1701-4 (Fig. 7a) is almost constant, while it shows a subtle increase in the law-BS sample L1413-8B (Fig. 7d).

### 5.2. Omphacite

Clinopyroxene in the three eclogites varies widely in composition (Tables 1 and 2; Fig. 7f). It mostly belongs to omphacite in the Q-Jd-Aeg diagram (Morimoto et al., 1988) with only one exception (Fig. 7f, aegirine-augite). Omphacite in the ep-EC L1701-4 sample shows an obvious increase of the jadeite content and a sharp decrease of the wollastonite + enstatite + ferrosilite (Q) content from inclusions enclosed in garnet ($Jd_{18.0–27.2}Q_{55.1–69.4}Aeg_{12.1–24.1}$) to their matrix counterparts ($Jd_{25.9–39.8}Q_{54.9–60.4}Aeg_{4.3–19.2}$). Omphacite in the Law-EC sample L1413-3 shares the same compositional range and trend as the inclusions ($Jd_{14.3–27.9}Q_{56.6–77.5}Aeg_{7.9–21.7}$) and matrix grains ($Jd_{30.0–41.2}Q_{54.8–63.8}Aeg_{1.2–7.8}$). In the Law-EC sample L1413-11, omphacite inclusions in garnet have similar jadeite but slightly higher aegirine contents ($Jd_{20.2–22.4}Q_{60.3–64.6}Aeg_{15.2–17.3}$) compared to the inclusion omphacite in the samples L1701-4 and L1413-3.

### 5.3. Lawsonite

Lawsonite in both law-EC and law-BS samples has compositions close to its ideal formula $CaAl_2(H_2O)[Si_2O_7](OH)_2$ (Tables 2 and 3). The $FeO^T$ content is 1.06–1.79 wt. %, which is higher than the lawsonite in the lawsonite-glaucophane-bearing but garnet-absent blueschists from the Hongjishan area, Qiangtang Terrane (Tang & Zhang, 2014) and the SW Tianshan, Xinjiang (Du et al., 2011); but is similar to the lawsonite in the law-BS and law-EC from other areas (Ao & Bhowmik, 2014; Du et al., 2014c; Whitney et al., 2020).

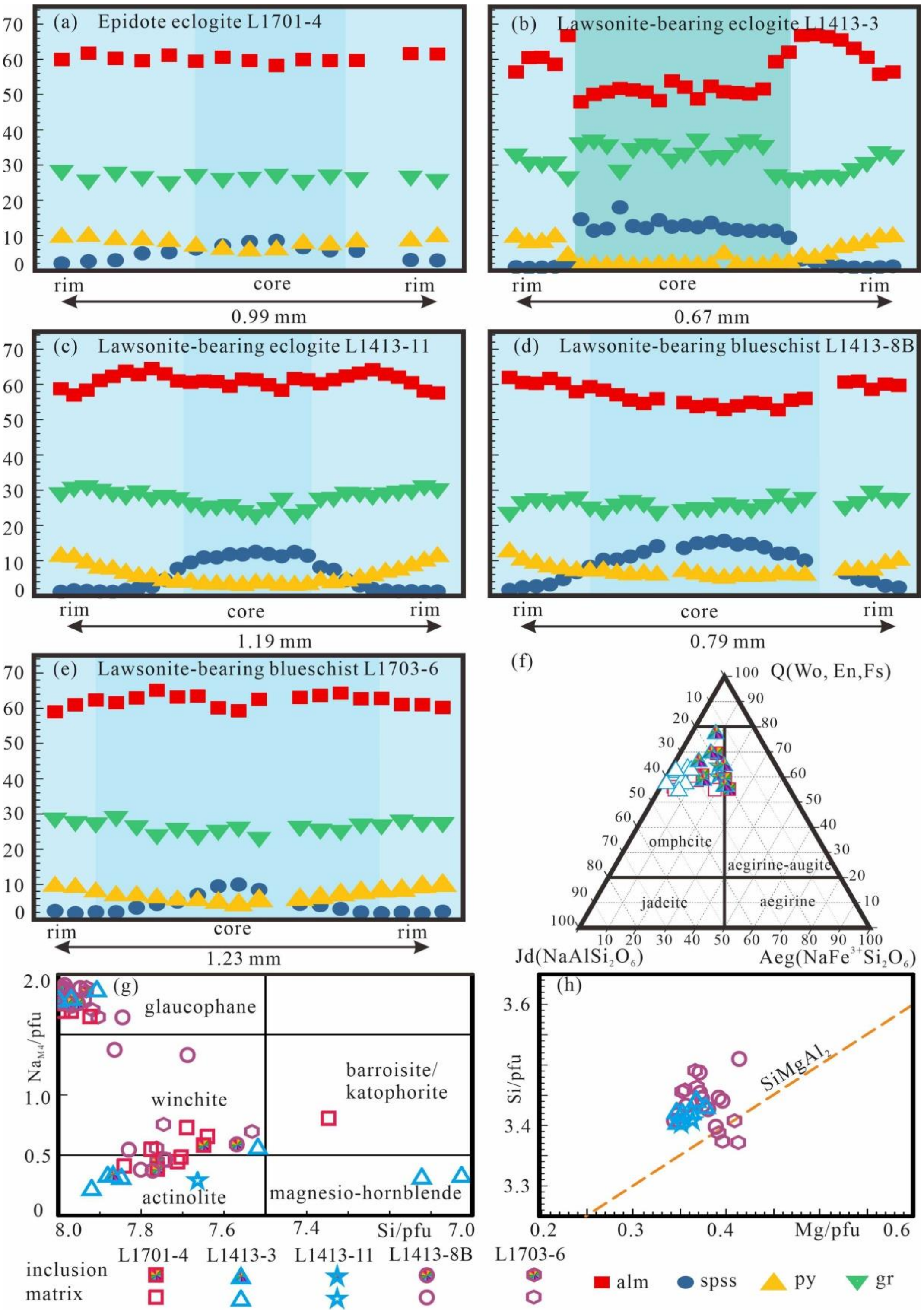


Fig. 7. Compositional diagrams showing variations of garnet (a–e), clinopyroxene (f; Morimoto et al., 1988), amphibole (g; Leake et al., 1997)) and phengite (h). Profiles of garnet correspond to pink lines in Figs. 4b, 5a, h and 6a, e for relevant samples.

Table 1. Representative chemical compositions of minerals in the epidote eclogite L1701-4.

| | g-c | g-r | o-I | o-M | gl-I | gl-M | aln | ep | hb | act |
|---|---|---|---|---|---|---|---|---|---|---|
| $SiO_2$ | 37.24 | 37.45 | 53.89 | 54.32 | 57.53 | 56.77 | 34.75 | 38.13 | 53.38 | 54.90 |

| | | | | | | | | | | |
|---|---|---|---|---|---|---|---|---|---|---|
| $TiO_2$ | 0.17 | 0.11 | 0.55 | 0.08 | 0.01 | 0.00 | 0.00 | 0.18 | 0.08 | 0.01 |
| $Al_2O_3$ | 20.65 | 20.97 | 5.46 | 6.30 | 9.74 | 10.35 | 19.71 | 26.77 | 5.30 | 2.66 |
| $Cr_2O_3$ | 0.02 | 0.00 | 0.01 | 0.02 | 0.01 | 0.00 | 0.00 | 0.03 | 0.00 | 0.13 |
| FeO | 26.98 | 27.66 | 12.63 | 10.72 | 11.12 | 10.18 | 13.01 | 8.39 | 11.65 | 10.43 |
| MnO | 3.61 | 1.18 | 0.20 | 0.16 | 0.04 | 0.03 | 0.11 | 0.05 | 0.05 | 0.06 |
| MgO | 1.43 | 2.48 | 7.55 | 7.97 | 10.73 | 10.39 | 0.04 | 0.07 | 14.76 | 16.58 |
| CaO | 9.20 | 8.98 | 13.32 | 13.50 | 1.58 | 1.46 | 18.67 | 22.30 | 8.16 | 9.82 |
| $Na_2O$ | 0.02 | 0.02 | 6.35 | 6.24 | 6.46 | 6.19 | 0.01 | 0.00 | 2.82 | 1.71 |
| $K_2O$ | 0.00 | 0.00 | 0.00 | 0.00 | 0.02 | 0.01 | 0.01 | 0.01 | 0.09 | 0.06 |
| Totals | 99.35 | 98.84 | 99.96 | 99.31 | 97.24 | 95.38 | 86.31 | 95.93 | 96.29 | 96.36 |
| Oxygen | 12.00 | 12.00 | 6.00 | 6.00 | 23.00 | 23.00 | 12.50 | 12.50 | 23.00 | 23.00 |
| Si | 3.00 | 3.00 | 1.97 | 1.99 | 7.97 | 7.99 | 3.09 | 3.02 | 7.64 | 7.84 |
| Ti | 0.01 | 0.01 | 0.02 | 0.00 | 0.00 | 0.00 | 0.00 | 0.01 | 0.01 | 0.00 |
| Al | 1.96 | 1.98 | 0.24 | 0.27 | 1.59 | 1.72 | 2.06 | 2.50 | 0.89 | 0.45 |
| Cr | 0.00 | 0.00 | 0.00 | 0.00 | 0.00 | 0.00 | 0.00 | 0.00 | 0.00 | 0.02 |
| $Fe^{3+}$ | 0.03 | 0.00 | 0.24 | 0.19 | 0.12 | 0.00 | 0.94 | 0.49 | 0.32 | 0.19 |
| $Fe^{2+}$ | 1.79 | 1.86 | 0.15 | 0.14 | 1.17 | 1.20 | 0.03 | 0.06 | 1.07 | 1.06 |
| Mn | 0.25 | 0.08 | 0.01 | 0.01 | 0.01 | 0.00 | 0.01 | 0.00 | 0.01 | 0.01 |
| Mg | 0.17 | 0.30 | 0.41 | 0.43 | 2.22 | 2.18 | 0.01 | 0.01 | 3.15 | 3.53 |
| Ca | 0.79 | 0.77 | 0.52 | 0.53 | 0.24 | 0.22 | 1.78 | 1.89 | 1.25 | 1.50 |
| Na | 0.00 | 0.00 | 0.45 | 0.44 | 1.74 | 1.69 | 0.00 | 0.00 | 0.78 | 0.47 |
| K | 0.00 | 0.00 | 0.00 | 0.00 | 0.00 | 0.00 | 0.00 | 0.00 | 0.02 | 0.01 |
| Sum | 8.00 | 8.00 | 4.00 | 4.00 | 15.04 | 15.00 | 7.91 | 7.98 | 15.14 | 15.07 |
| X(phase) | 5.73 | 9.86 | 55.10 | 54.90 | 0.65 | 0.65 | 31.20 | 16.47 | 0.75 | 0.77 |
| Y(phase) | 26.44 | 25.71 | 20.80 | 25.90 | 1.70 | 1.69 | | | 0.66 | 0.43 |
| Z(phase) | 8.19 | 2.66 | 24.10 | 19.20 | | | | | | |

-c, core; -r, rim; -I, inclusions in garnet; -M, minerals in the matrix; X(g) = py = Mg/(Ca + Mg + Mn + $Fe^{2+}$)×100; Y(g) = gr = Ca/(Ca + Mg + Mn + $Fe^{2+}$)×100; Z(g) = spss = Mn/(Ca + Mg + Mn + $Fe^{2+}$)×100; X(o) = WEF; Y(o) = Jd; Z(o) = Aeg; X(gl/hb/act) = $X_{Mg}$ = Mg/($Fe^{2+}$ + Mg); Y(gl/hb/act) = $Na_{M4}$; X(ep/aln) = Ps = $Fe^{3+}$/($Fe^{3+}$ + Al)×100. The mineral formulae and ferric iron were calculated using the program AX (Holland; https://www.esc.cam.ac.uk/research/research-groups/research-projects/tim-hollands-software-pages/ax).

Table 2. Representative chemical compositions of minerals in the lawsonite-bearing eclogites L1413-3 and L1413-11 from the Lanling area, central Qiangtang Terrane.

| | L1413-3 | | | | | | | | | | L1413-11 | | | | | | | |
|---|---|---|---|---|---|---|---|---|---|---|---|---|---|---|---|---|---|---|
| | g-c | g-r | o-I | o-M | gl-M | ep | act | hb | ph | law | g-c | g-r | o-I | gl-M | ep | act | ph | law |
| $SiO_2$ | 37.45 | 38.33 | 53.76 | 56.38 | 58.16 | 39.17 | 55.41 | 52.84 | 50.87 | 38.88 | 36.97 | 37.90 | 53.76 | 57.97 | 38.57 | 53.14 | 50.65 | 37.88 |
| $TiO_2$ | 0.10 | 0.02 | 0.44 | 0.04 | 0.00 | 0.11 | 0.00 | 0.18 | 0.15 | 0.03 | 0.06 | 0.08 | 0.03 | 0.03 | 0.25 | 0.00 | 0.08 | 0.00 |
| $Al_2O_3$ | 20.54 | 21.56 | 4.14 | 9.82 | 12.29 | 29.24 | 2.01 | 6.71 | 26.45 | 31.91 | 20.89 | 21.18 | 4.61 | 11.28 | 27.65 | 4.56 | 27.03 | 31.51 |
| $Cr_2O_3$ | 0.05 | 0.06 | 0.23 | 0.84 | 0.40 | 0.06 | 0.44 | 0.44 | 0.24 | 0.06 | 0.00 | 0.13 | 0.00 | 0.04 | 0.11 | 0.03 | 0.03 | 0.06 |
| FeO | 24.34 | 25.71 | 8.54 | 4.85 | 8.51 | 5.37 | 10.31 | 9.74 | 2.31 | 1.68 | 27.66 | 26.78 | 12.00 | 8.83 | 6.74 | 10.74 | 1.97 | 1.40 |
| MnO | 5.70 | 0.52 | 0.13 | 0.07 | 0.00 | 0.02 | 0.05 | 0.00 | 0.00 | 0.03 | 5.38 | 0.46 | 0.07 | 0.03 | 0.00 | 0.13 | 0.03 | 0.06 |
| MgO | 0.44 | 2.49 | 11.03 | 8.11 | 10.59 | 0.08 | 16.73 | 14.92 | 3.46 | 0.04 | 0.72 | 2.84 | 8.08 | 10.60 | 0.24 | 15.15 | 3.51 | 0.02 |
| CaO | 11.66 | 11.60 | 19.21 | 13.77 | 0.66 | 23.82 | 10.64 | 9.19 | 0.04 | 17.56 | 7.92 | 10.29 | 15.33 | 1.00 | 23.42 | 10.99 | 0.00 | 17.09 |
| $Na_2O$ | 0.00 | 0.00 | 3.11 | 6.65 | 7.13 | 0.00 | 1.34 | 2.58 | 0.38 | 0.02 | 0.02 | 0.01 | 4.97 | 6.75 | 0.00 | 1.50 | 0.43 | 0.03 |
| $K_2O$ | 0.00 | 0.00 | 0.00 | 0.00 | 0.05 | 0.03 | 0.17 | 0.22 | 10.86 | 0.01 | 0.05 | 0.00 | 0.01 | 0.00 | 0.00 | 0.13 | 11.16 | 0.01 |
| Totals | 100.28 | 100.29 | 100.59 | 100.53 | 97.79 | 97.90 | 97.10 | 96.82 | 94.76 | 90.22 | 99.67 | 99.67 | 98.86 | 96.53 | 96.98 | 96.37 | 94.89 | 88.06 |
| Oxygen | 12.00 | 12.00 | 6.00 | 6.00 | 23.00 | 12.50 | 23.00 | 23.00 | 11.00 | 8.00 | 12.00 | 12.00 | 6.00 | 23.00 | 12.50 | 23.00 | 11.00 | 8.00 |
| Si | 2.99 | 3.01 | 1.97 | 2.01 | 7.91 | 3.01 | 7.88 | 7.52 | 3.42 | 2.01 | 2.99 | 3.00 | 2.00 | 7.99 | 3.01 | 7.66 | 3.40 | 2.01 |
| Ti | 0.01 | 0.00 | 0.01 | 0.00 | 0.00 | 0.01 | 0.00 | 0.02 | 0.01 | 0.00 | 0.00 | 0.01 | 0.00 | 0.00 | 0.02 | 0.00 | 0.00 | 0.00 |
| Al | 1.94 | 1.99 | 0.18 | 0.41 | 1.97 | 2.65 | 0.34 | 1.13 | 2.10 | 1.95 | 1.99 | 1.98 | 0.20 | 1.83 | 2.54 | 0.78 | 2.14 | 1.97 |
| Cr | 0.00 | 0.00 | 0.01 | 0.02 | 0.04 | 0.00 | 0.05 | 0.05 | 0.01 | 0.00 | 0.00 | 0.01 | 0.00 | 0.00 | 0.01 | 0.00 | 0.00 | 0.00 |
| $Fe^{3+}$ | 0.07 | 0.00 | 0.08 | 0.01 | 0.03 | 0.34 | 0.12 | 0.13 | 0.00 | 0.00 | 0.04 | 0.01 | 0.15 | 0.00 | 0.44 | 0.04 | 0.00 | 0.00 |
| $Fe^{2+}$ | 1.56 | 1.69 | 0.18 | 0.13 | 0.94 | 0.00 | 1.11 | 1.03 | 0.13 | 0.07 | 1.83 | 1.76 | 0.22 | 1.02 | 0.00 | 1.26 | 0.11 | 0.06 |

| | | | | | | | | | | | | | | | | | | |
|---|---|---|---|---|---|---|---|---|---|---|---|---|---|---|---|---|---|---|
| Mn | 0.39 | 0.04 | 0.00 | 0.00 | 0.00 | 0.00 | 0.01 | 0.00 | 0.00 | 0.00 | 0.37 | 0.03 | 0.00 | 0.00 | 0.00 | 0.02 | 0.00 | 0.00 |
| Mg | 0.05 | 0.29 | 0.60 | 0.43 | 2.15 | 0.01 | 3.55 | 3.16 | 0.35 | 0.00 | 0.09 | 0.34 | 0.45 | 2.18 | 0.03 | 3.26 | 0.35 | 0.00 |
| Ca | 1.00 | 0.98 | 0.75 | 0.53 | 0.10 | 1.96 | 1.62 | 1.40 | 0.00 | 0.97 | 0.69 | 0.87 | 0.61 | 0.15 | 1.96 | 1.70 | 0.00 | 0.97 |
| Na | 0.00 | 0.00 | 0.22 | 0.46 | 1.88 | 0.00 | 0.37 | 0.71 | 0.05 | 0.00 | 0.00 | 0.00 | 0.36 | 1.81 | 0.00 | 0.42 | 0.06 | 0.00 |
| K | 0.00 | 0.00 | 0.00 | 0.00 | 0.01 | 0.00 | 0.03 | 0.04 | 0.93 | 0.00 | 0.01 | 0.00 | 0.00 | 0.00 | 0.00 | 0.02 | 0.96 | 0.00 |
| Sum | 8.00 | 7.99 | 4.00 | 4.00 | 15.02 | 7.99 | 15.07 | 15.23 | 7.01 | 5.00 | 8.00 | 8.00 | 4.00 | 14.99 | 7.99 | 15.16 | 7.03 | 5.01 |
| X(phase) | 1.73 | 9.74 | 77.50 | 57.60 | 0.70 | 11.40 | 0.76 | 0.75 | | | 2.92 | 11.16 | 64.60 | 0.68 | 14.62 | 0.72 | | |
| Y(phase) | 33.29 | 32.63 | 14.30 | 41.20 | 1.87 | | 0.33 | 0.56 | | | 23.06 | 29.06 | 20.20 | 1.82 | | 0.29 | | |
| Z(phase) | 12.88 | 1.17 | 8.20 | 1.20 | | | | | | | 12.37 | 1.03 | 15.20 | | | | | |

Lawsonite is normalized to eight oxygen and total Fe is regarded as $Fe^{2+}$. Others are same as in Table 1.

Table 3. Representative chemical compositions of minerals in the lawsonite-bearing blueschists L1413-8B and L1703-6 from the Lanling area, central Qiangtang Terrane.

| | L1413-8B | | | | | | | | | L1703-6 | | | | | | | |
|---|---|---|---|---|---|---|---|---|---|---|---|---|---|---|---|---|---|
| | g-c | g-r | gl-I | gl-M | hb | ep | ph | law | chl | g-c | g-r | gl-I | gl-M | hb | ep | ph | law |
| $SiO_2$ | 37.44 | 37.94 | 57.39 | 57.50 | 54.50 | 38.04 | 49.94 | 37.83 | 25.80 | 37.05 | 38.21 | 55.59 | 55.62 | 53.42 | 38.54 | 51.47 | 38.29 |
| $TiO_2$ | 0.13 | 0.02 | 0.09 | 0.00 | 0.04 | 0.16 | 0.19 | 0.00 | 0.06 | 0.17 | 0.05 | 0.01 | 0.03 | 0.03 | 0.05 | 0.16 | 0.00 |
| $Al_2O_3$ | 20.26 | 21.35 | 10.25 | 10.23 | 3.70 | 26.21 | 25.21 | 31.55 | 18.14 | 20.29 | 21.35 | 9.26 | 8.82 | 4.03 | 26.09 | 25.26 | 31.77 |
| $Cr_2O_3$ | 0.03 | 0.14 | 0.01 | 0.03 | 0.03 | 0.07 | 0.27 | 0.09 | 0.23 | 0.00 | 0.04 | 0.00 | 0.00 | 0.05 | 0.06 | 0.01 | 0.00 |
| FeO | 24.77 | 28.29 | 9.24 | 9.24 | 10.72 | 8.35 | 2.79 | 1.16 | 17.40 | 27.06 | 27.13 | 11.39 | 11.06 | 10.32 | 8.85 | 2.16 | 1.16 |
| MnO | 6.94 | 0.78 | 0.04 | 0.02 | 0.18 | 0.03 | 0.03 | 0.05 | 0.09 | 4.38 | 1.03 | 0.04 | 0.04 | 0.07 | 0.06 | 0.05 | 0.03 |
| MgO | 1.29 | 3.21 | 10.85 | 11.05 | 15.27 | 0.11 | 3.67 | 0.00 | 19.76 | 1.11 | 2.51 | 9.79 | 11.15 | 15.43 | 0.06 | 3.63 | 0.01 |

| | | | | | | | | | | | | | | | | | |
|---|---|---|---|---|---|---|---|---|---|---|---|---|---|---|---|---|---|
| CaO | 9.22 | 8.37 | 0.78 | 0.43 | 9.16 | 23.25 | 0.00 | 16.72 | 0.00 | 9.07 | 9.67 | 0.45 | 1.90 | 8.83 | 24.17 | 0.01 | 16.04 |
| $Na_2O$ | 0.00 | 0.00 | 7.04 | 7.21 | 2.22 | 0.02 | 3.67 | 0.01 | 0.01 | 0.03 | 0.01 | 6.87 | 6.40 | 2.29 | 0.03 | 0.26 | 0.00 |
| $K_2O$ | 0.00 | 0.01 | 0.03 | 0.01 | 0.10 | 0.00 | 10.67 | 0.01 | 0.00 | 0.01 | 0.01 | 0.00 | 0.00 | 0.07 | 0.00 | 10.70 | 0.00 |
| Totals | 100.08 | 100.11 | 95.72 | 95.72 | 95.92 | 96.24 | 96.44 | 87.42 | 81.49 | 99.17 | 100.01 | 93.40 | 95.02 | 94.54 | 97.91 | 93.71 | 87.30 |
| Oxygen | 12.00 | 12.00 | 23.00 | 23.00 | 23.00 | 12.50 | 11.00 | 8.00 | 14.00 | 12.00 | 12.00 | 23.00 | 23.00 | 23.00 | 12.50 | 11.00 | 8.00 |
| Si | 3.00 | 3.00 | 7.99 | 7.99 | 7.83 | 3.01 | 3.43 | 2.02 | 2.82 | 3.01 | 3.02 | 7.99 | 7.90 | 7.76 | 3.00 | 3.49 | 2.03 |
| Ti | 0.01 | 0.00 | 0.01 | 0.00 | 0.00 | 0.01 | 0.01 | 0.00 | 0.01 | 0.01 | 0.00 | 0.00 | 0.00 | 0.00 | 0.00 | 0.01 | 0.00 |
| Al | 1.91 | 1.99 | 1.68 | 1.68 | 0.63 | 2.44 | 2.04 | 1.96 | 2.34 | 1.92 | 1.99 | 1.57 | 1.48 | 0.69 | 2.40 | 2.02 | 1.99 |
| Cr | 0.00 | 0.01 | 0.00 | 0.00 | 0.00 | 0.00 | 0.02 | 0.00 | 0.02 | 0.00 | 0.00 | 0.00 | 0.00 | 0.01 | 0.00 | 0.00 | 0.00 |
| $Fe^{3+}$ | 0.07 | 0.01 | 0.15 | 0.23 | 0.16 | 0.52 | 0.00 | 0.00 | 0.00 | 0.05 | 0.00 | 0.33 | 0.23 | 0.23 | 0.57 | 0.00 | 0.00 |
| $Fe^{2+}$ | 1.59 | 1.86 | 0.93 | 0.84 | 1.13 | 0.03 | 0.16 | 0.07 | 1.59 | 1.78 | 1.79 | 1.04 | 1.08 | 1.02 | 0.01 | 0.12 | 0.05 |
| Mn | 0.47 | 0.05 | 0.01 | 0.00 | 0.02 | 0.00 | 0.00 | 0.00 | 0.01 | 0.30 | 0.07 | 0.01 | 0.01 | 0.01 | 0.00 | 0.00 | 0.00 |
| Mg | 0.15 | 0.38 | 2.25 | 2.29 | 3.27 | 0.01 | 0.38 | 0.00 | 3.22 | 0.13 | 0.30 | 2.10 | 2.36 | 3.34 | 0.01 | 0.37 | 0.00 |
| Ca | 0.79 | 0.71 | 0.12 | 0.06 | 1.41 | 1.97 | 0.00 | 0.94 | 0.00 | 0.79 | 0.82 | 0.07 | 0.29 | 1.38 | 2.02 | 0.00 | 0.91 |
| Na | 0.00 | 0.00 | 1.90 | 1.94 | 0.62 | 0.00 | 0.05 | 0.00 | 0.00 | 0.00 | 0.00 | 1.92 | 1.76 | 0.64 | 0.00 | 0.04 | 0.00 |
| K | 0.00 | 0.00 | 0.01 | 0.00 | 0.02 | 0.00 | 0.94 | 0.00 | 0.00 | 0.00 | 0.00 | 0.00 | 0.00 | 0.01 | 0.00 | 0.93 | 0.00 |
| Sum | 8.00 | 8.00 | 15.04 | 15.03 | 15.09 | 8.00 | 7.02 | 4.99 | 10.00 | 8.00 | 7.99 | 15.02 | 15.12 | 15.10 | 8.01 | 6.97 | 4.98 |
| X(phase) | 5.12 | 12.62 | 0.71 | 0.73 | 0.74 | 17.67 | | | 0.67 | 4.46 | 9.92 | 0.67 | 0.69 | 0.77 | 19.25 | | |
| Y(phase) | 26.33 | 23.64 | 1.87 | 1.91 | 0.55 | | | | | 26.22 | 27.51 | 1.90 | 1.65 | 0.56 | | | |
| Z(phase) | 15.66 | 1.74 | | | | | | | | 10.02 | 2.32 | | | | | | |

X(chl) = $Mg^{\#}$ = Mg/(Mg + $Fe^{2+}$). Others are same as in Table 1 and Table 2.

### 5.4. Amphibole

Glaucophane varies slightly in compositions among all five studied samples (Si = 7.91–8.00 pfu, $Na_{M4}$ = 1.64–1.91 pfu, $(Na + K)_A$ = 0–0.12 pfu and $X_{Mg}$ = 0.63–0.73; Fig. 7g). Glaucophane in the ep-EC sample L1701-4 exhibits a decrease of $Na_{M4}$ content from the inclusions enclosed in garnet (~1.78 pfu) to the matrix grains (1.65–1.78 pfu), which is a little lower than the matrix glaucophane of the law-EC samples L1413-3 (1.80–1.87 pfu) and L1413-11 (~1.82 pfu). The glaucophane inclusions in garnet from the Law-BS sample L1413-8B and L1703-6 show narrower ranges of $Na_{M4}$ content (1.74–1.80 and 1.85–1.90 pfu) than their corresponding matrix grains (1.64–1.91 and 1.65–1.89 pfu). According to Leake et al. (1997), the sodic-calcic amphibole is barroisite and winchite and the calcic amphibole is actinolite and magnesio-horblende (Fig. 7g). Horblende/actinolite in the ep-EC sample L1701-4 varies more widely in the $Na_{M4}$ content (0.38–0.81 pfu) compared to Si = 7.35–7.84 pfu, $(Na + K)_A$ = 0.07–0.15 pfu, and $X_{Mg}$ = 0.70–0.77. In contrast, horblende/actinolite in the law-EC samples L1413-3 and L1413-11 varies more widely in the Si content (7.03–7.92 pfu) compared to $Na_{M4}$ = 0.29–0.56 pfu, $(Na + K)_A$ = 0.03–0.41 pfu, and $X_{Mg}$ = 0.54–0.78. Horblende/actinolite in the law-BS samples L1413-8B and L1703-6 has similar compositions to that in the ep-EC sample L1701-4 (Si = 7.53–7.80 pfu, $Na_{M4}$ = 0.37–1.33 pfu, $(Na + K)_A$ = 0.09–0.22 pfu, and $X_{Mg}$ = 0.67–0.79).

### 5.5. White mica, epidote/allanite, albite and chlorite

White mica includes phengite and paragonite. Phengite in the law-BS samples L1413-8B and L1703-6 has slightly higher Si contents (3.40–3.51 and 3.37–3.49 pfu; Fig. 7h) than that of the Law-EC samples L1413-3 and L1413-11 (3.41–3.44 and 3.40–3.41 pfu). Phengite shares the same composition range as that in the garnet blueschists (3.38–3.49 pfu) from the same area (Liu et al., 2011; Wang et al., 2018). Paragonite and albite have compositions close to their pure end-members. Epidote from all samples has no significant differences in compositions. The pistacite (Ps) content ranges from 11.4 to 23.8 mol. %. Allanite from the ep-EC sample L1701-4 has a Ps content of ~31.2 mol. %. Chlorite has a narrow $Mg^{\#}$ in the range of 0.64–0.67.

## 6. Phase equilibria modeling

Each P-T pseudosection (Figs. 8 and S2) is contoured with the isopleths of grossular and pyrope percentages of garnet and Si number pfu of phengite, except the ep-EC sample L1701-4. For each sample, the core (blue circles) and rim (white squares) compositions of garnet were plotted based on the intersections of their measured grossular and pyrope contents (Figs. 8 and S2) in the P-T pseudosections, which are constructed using both the unfractionated and fractionated effective bulk-rock compositions (Table 4).

Table 4. Bulk-rock compositions of eclogites and blueschists from the Lanling area, central Qiangtang Terrane.

| Sample | $TiO_2$ | $SiO_2$ | $Al_2O_3$ | $Fe_2O_3$ | FeO | CaO | MgO | $K_2O$ | $Na_2O$ | MnO | $P_2O_5$ | LOI | Total |
|---|---|---|---|---|---|---|---|---|---|---|---|---|---|
| XRF analyses (wt. %) | | | | | | | | | | | | | |
| L1701-4 | 1.17 | 47.62 | 14.47 | 6.03 | 5.13 | 14.87 | 5.92 | 0.09 | 2.67 | 0.17 | 0.16 | 1.60 | 99.90 |
| L1413-3 | 1.46 | 47.77 | 14.36 | 2.59 | 9.53 | 11.05 | 7.23 | 0.79 | 2.02 | 0.21 | 0.14 | 2.72 | 99.87 |
| L1413-11 | 1.46 | 49.42 | 14.23 | 3.08 | 8.29 | 10.82 | 7.59 | 0.43 | 1.88 | 0.17 | 0.15 | 2.33 | 99.87 |
| L1414-1* | 1.85 | 47.66 | 14.04 | 5.28 | 9.62 | 4.84 | 7.70 | 0.16 | 4.14 | 1.24 | 0.19 | 3.12 | 99.84 |
| L1414-7* | 0.66 | 73.54 | 13.56 | 0.79 | 3.32 | 0.49 | 1.27 | 1.95 | 1.89 | 0.04 | 0.08 | 2.31 | 99.89 |
| | Model system | Si | Al | $Fe^{3+}$ | $Fe^{2+}$ | Ca | Mg | K | Na | Mn | O | | |
| Unfractionated bulk compositions | | | | | | | | | | | | | |
| L1701-4 | MnNCFMASHO | 46.358 | 16.462 | 3.791 | 3.701 | 15.404 | 7.437 | | 6.743 | 0.104 | 153.113 | | |
| L1413-3 | MnNCKFMASHO | 43.909 | 22.861 | 1.018 | 13.319 | 11.706 | 3.051 | 0.893 | 1.526 | 1.718 | 154.640 | | |
| L1413-8B | MnNCKFMASHO | 50.565 | 14.382 | 1.492 | 6.891 | 12.288 | 4.156 | 0.124 | 9.844 | 0.258 | 153.658 | | |
| L1703-6 | MnNCKFMASHO | 48.854 | 15.939 | 1.766 | 8.263 | 6.216 | 10.416 | 0.119 | 8.197 | 0.230 | 153.549 | | |
| Fractionated bulk compositions | | | | | | | | | | | | | |
| L1701-4 | MnNCFMASHO | 46.538 | 16.296 | 3.855 | 3.324 | 15.512 | 7.510 | | 6.875 | 0.089 | 153.175 | | |
| L1413-3 | MnNCKFMASHO | 46.570 | 22.442 | 1.070 | 10.050 | 11.689 | 4.559 | 1.268 | 2.166 | 0.185 | 156.608 | | |
| L1413-8B | MnNCKFMASHO | 51.078 | 14.000 | 1.516 | 6.365 | 3.935 | 12.686 | 0.129 | 10.228 | 0.063 | 153.658 | | |
| L1703-6 | MnNCKFMASHO | 49.739 | 15.285 | 1.867 | 7.043 | 5.958 | 11.074 | 0.128 | 8.842 | 0.063 | 153.829 | | |

* come from Wang et al. (2018). The $H_2O$ content is assumed to be in excess.

### 6.1. P-T pseudosections of ep-EC

P-T pseudosections calculated for the ep-EC sample L1701-4 (Fig. 8a and b) with unfractionated and fractionated effective bulk-rock compositions (Table 4) exhibit similar topological relationships among relevant phases, except for the enlarged stability fields of glaucophane and talc in the fractionated pseudosection. Lawsonite is stable above 11–12 kbar at 400 °C and above 22 kbar at 600 °C, whereas epidote appears at lower pressures and higher temperatures. The observed matrix mineral assemblage including ep + g + o + gl + q corresponds to a P-T field of 11–21 kbar and >520 °C.

The measured core and rim compositions of garnet indicate a prograde P-T vector with heating decompression from ~23 kbar at ~480 °C (garnet core, pressure peak, i.e., $P_{max}$) to ~22 kbar at ~530 °C (garnet rim, temperature peak, i.e., $T_{max}$) (C → R in Fig. 8b). Garnet is predicted to grow in the mineral assemblages transitioning from g + o + gl + law + chl (+$H_2O$) to g + o + gl + law + chl + q (+$H_2O$). Subsequent exhumation is inferred to have experienced isothermal decompression, based on (i) the matrix mineral assemblage of ep + g + o + gl + q (Fig. 4a), (ii) the hornblende overgrowth on glaucophane (Fig. 4c), and (iii) the absence of diopside in the matrix.

### 6.2. P-T pseudosections of law-EC

Compared to ep-EC sample L1701-4, P-T pseudosections for the law-EC sample L1413-3 (Fig. 8c and d) show much larger stability fields of chlorite- (T<540 °C and P<25 kbar) and actinolite-bearing mineral assemblages (P > 21 kbar and T < 520 °C), but smaller stability fields of talc and omphacite. The observed matrix mineral assemblage of ep + g + o + gl + ph + q appears in a P-T field of 15–20 kbar and 530–600 °C (Fig. 8c and d).

The measured core compositions of garnet in the law-EC sample L1413-3 suggest roughly a prograde P-T vector with heating and burial from ~17.5 kbar at ~450 °C to ~22.5 kbar at ~475 °C ($P_{max}$) in the mineral assemblage g + o + gl +law + chl + q (+ ph + $H_2O$) (C0 → C in Fig. 8d). The measured mantle and rim compositions of garnet point to a P-T vector with heating decompression from ~22.5 kbar at ~475 °C to ~20.0 kbar at ~540 °C ($T_{max}$) corresponding to the mineral assemblage transition from g + o + gl +law + chl + q (+ ph + $H_2O$) to g + o + gl +law + q (+ ph + $H_2O$) (C → R in Fig.

8d). The measured Si content of phengite (3.41–3.44) indicates pressures of 21–22 kbar at ~540 °C. An isothermal decompression P-T vector is inferred for exhumation process after $T_{max}$, based on (i) the matrix mineral assemblage of ep + g + o + gl + ph + q (Fig. 5a, d), (ii) the hornblende overgrowth on glaucophane and omphacite (Fig. 5b, d), and (iii) the scarcity of omphacite and abundance of hornblende in the matrix.

The measured profile of garnet in the law-EC sample L1413-11, when plotted on P-T pseudosections of sample L1413-3 (Fig. S2a and b), reflects a P-T path with heating decompression from ~22.5 kbar at ~460 °C (garnet core, $P_{max}$) to ~21 kbar at ~540 °C (garnet rim, $T_{max}$) (C → R in Fig. S2b). The Si content of phengite (3.40–3.41) corresponds to ~20 kbar at ~540 °C. Notably, the zoning profiles of garnets in both law-EC samples L1413-3 and L1413-11 are plotted in the lawsonite- and omphacite-bearing assemblages g + o + gl + law +ph ± chl ± q, which agrees well with the presence of lawsonite and omphacite inclusions in the garnet.

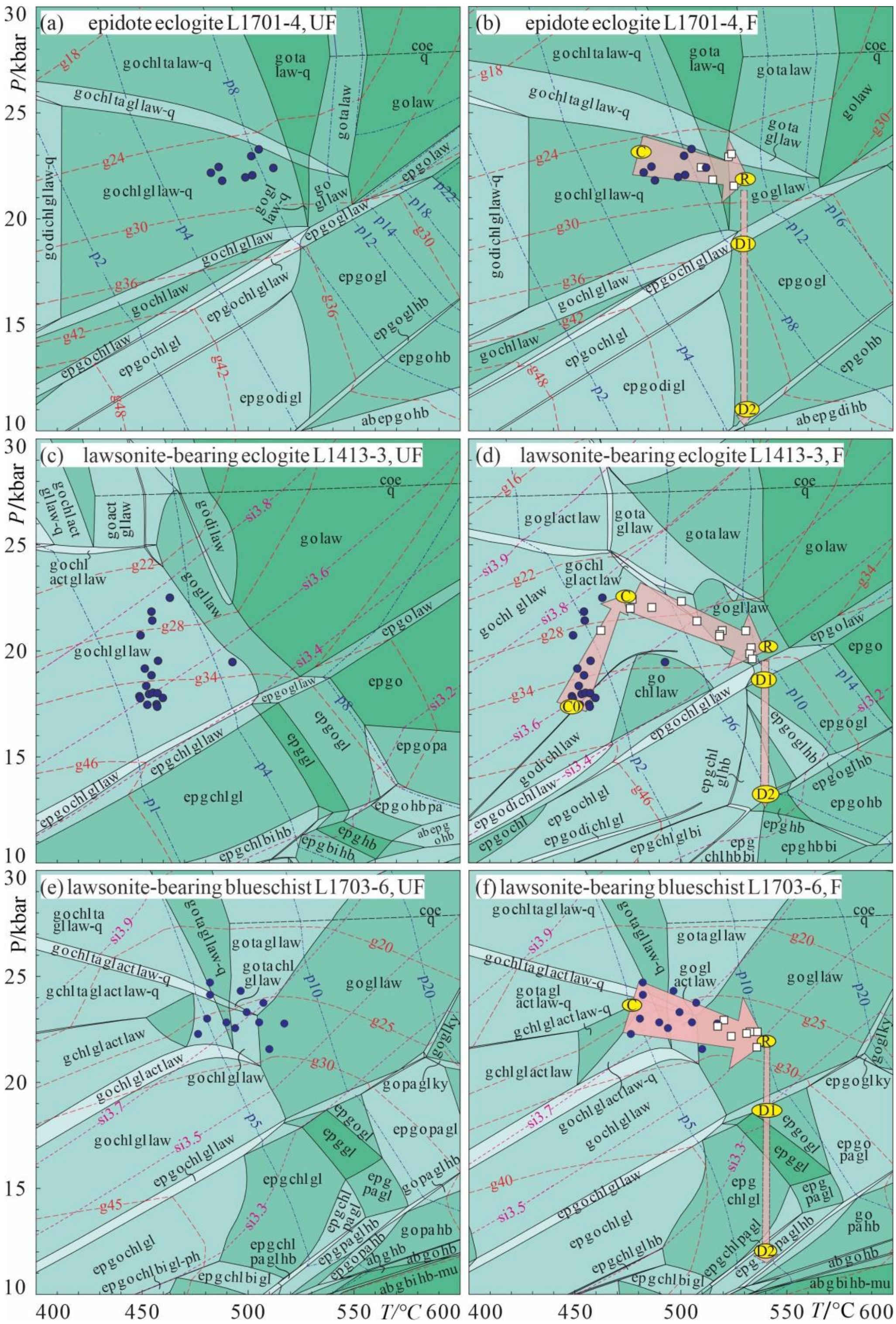


Fig. 8. P-T pseudosections calculated for the epidote eclogite L1701-4 (a, b), the lawsonite-bearing eclogite L1413-3 (c, d) and the lawsonite-bearing blueschist L1703-6 (e, f). (a, c, e) For unfractionated (UF) bulk compositions and (b, d, f) for fractionated (F) bulk compositions shown in table 4 with quartz, $H_2O$ and/or phengite in excess. The pseudosections are contoured with isopleths of the pyrope (p1–p22) and grossular (g18–g48) contents of garnet and Si (si3.2–si3.9) content of phengite. The blue circles correspond to the core compositions of garnet plotted in the unfractionated *P-T* pseudosections (a, c e, also shown in b, d, f), while the white squares

correspond to the rim compositions of garnet plotted in the fractionated *P-T* pseudosection (b, d, f). Pink arrows stand for the derived P-T paths. The yellow circles with the labels C0, C, R, D1 and D2 mark stages of metamorphism.

### 6.3 P-T pseudosections of law-BS

P-T pseudosections calculated for the law-BS sample L1703-6 with unfractionated and fractionated effective bulk-rock compositions are presented in Fig. 8e and f, respectively. The observed matrix assemblage of ep + g + gl + ph + q corresponds to a P-T field of 15–19 kbar and 530–570 °C. The measured garnet profile reflects a heating decompression P-T path from ~23.5 kbar at ~475 °C (garnet core, $P_{max}$) to ~22 kbar at ~540 °C (garnet rim, $T_{max}$) with the mineral assemblages varying from g + o + gl + law + chl + act (+ ph + q + $H_2O$) to g + o + gl + law (+ ph + q + $H_2O$) (C → R in Fig. 8f). The measured Si content of phengite (3.37–3.49) points to P-T condition of 20–22 kbar and ~540 °C, marginally lower than that indicated by the garnet rim compositions. Subsequent exhumation after $T_{max}$ is inferred to have experienced isothermal decompression, based on (i) the presence of matrix assemblage of ep + g + gl + ph + q (Fig. 6f) and (ii) the hornblende overgrowth on glaucophane (Fig. 6e).

P-T pseudosections calculated for the law-BS sample L1413-8B using unfractionated and fractionated effective bulk-rock compositions are presented in Fig. S2c and d, respectively. The observed matrix assemblage of ep + g + pa + gl + ph + q refers to a P-T field of 14–19 kbar and 530–570 °C. The measured core and rim compositions of garnet correspond to a prograde P-T path with heating decompression from ~23.5 kbar at ~480 °C (garnet core, $P_{max}$) to ~22.5 kbar at ~550 °C (garnet rim, $T_{max}$) (C → R in Fig. S2d). Garnet is predicted to develop in the Law-bearing assemblages that changes from g + gl + law ± act ± chl ± ta (+ ph + q + $H_2O$) to g + o + gl + law (+ ph + q + $H_2O$), in agreement with the appearance of lawsonite inclusions in garnet. The measured Si content of phengite (3.41–3.51) points to pressures of 21.5–23.5 kbar at ~550 °C. A subsequent isothermal decompression P-T path similar to the sample L1703-6 is also inferred.

### 6.4. Density and net buoyancy variations of LT/HP rocks in the Lanling area

Density contoured P-T-ρ, P-Δρ and P-ρ diagrams are presented in Figs. 9, 10 and S3. The densities of the law-EC, ep-EC and law-BS (samples L1413-3, L1701-4, and L1414-1) vary in the range of 2.627–3.583 g·cm$^{-3}$, which are comparable to those calculated for a representative MORB composition (Wang et al., 2019). The densities of our samples strongly and positively correlate with temperature above 15 kbar and 450 °C, while outside this P-T field they are mainly increases with pressure (Fig. 9a–c). Along the P-T path derived for eclogites and blueschists in the core of Lanling area (Fig. 11; see discussion below), their density and net buoyancy variations generally exhibit four stages.

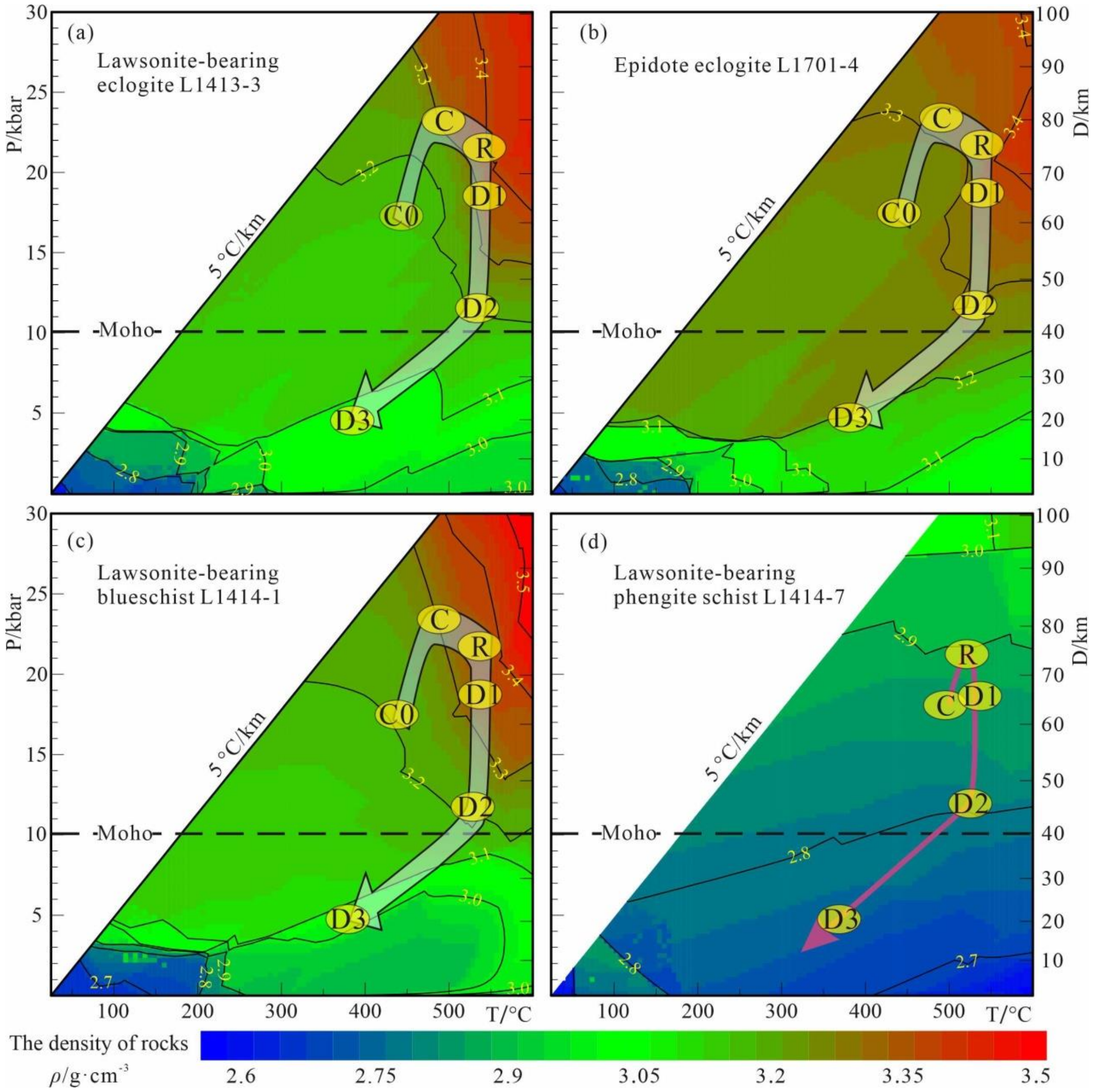


Fig. 9. P-T-ρ diagrams with density contours (2.7-3.5 g·cm$^{-3}$) calculated for LT/HP rocks in the core of the Lanling area, Central Qiangtang Terrane. (a) The lawsonite-bearing eclogite L1413-3; (b) the epidote eclogite L1701-4; (c) the lawsonite-bearing blueschist L1414-1 (Wang et al., 2018); (d) the lawsonite-bearing phengite schist L1414-7 (Wang et al., 2018). The P-T paths (Fig. 11) of eclogites and blueschists (translucent arrow) and lawsonite-bearing phengite schist (red arrow) are also shown.

During prograde burial (stage 1: C0→C in Figs. 8, 9a–c and S3), the densities increase gradually from 3.185–3.261 to 3.236–3.304 g·cm$^{-3}$ but are still much lower than that of the surrounding mantle derived from the Preliminary Reference Earth Model (PREM: 3.372–3.379 g·cm$^{-3}$ at pressures of 10–30 kbar; Fig. S3; Dziewonski & Anderson, 1981). Therefore, the eclogites and blueschists have positive net buoyancies (Δρ=0.071–0.192 g·cm$^{-3}$; Fig. 10a).

During heating decompression and early-stage isothermal decompression (stage 2: C→R→D1), the densities increase abruptly and exceed that of the PREM mantle (3.380–3.395 g·cm$^{-3}$) around $T_{max}$ (Figs. 9 and S3). It results in an abrupt net buoyancy decrease, to values equal to or less than zero (−0.020 to −0.004 g·cm$^{-3}$; Fig. 10).

During later-stage isothermal decompression (stage 3: D1→D2) and cooling decompression (stage 4: D2→D3), the densities decrease gradually to 3.022–3.190 g·cm$^{-3}$ at the position D3 (Figs. 9 and S3). Consequently, the net buoyancies become positive during later-stage isothermal decompression and reach the maximum at the position D2 (Δρ=0.189–0.206 g·cm$^{-3}$, Fig. 10a). As cooling decompression proceeds across the Moho discontinuity depth, the net buoyancies return to negative again and remain constant or increase subtly towards the Conrad discontinuity depth (Δρ=−0.159 to −0.381 g·cm$^{-3}$, Fig. 10a). As the decompression P-T path crosses over the Conrad discontinuity depth, the net buoyancies decrease further to −0.422 to −0.675 g·cm$^{-3}$.

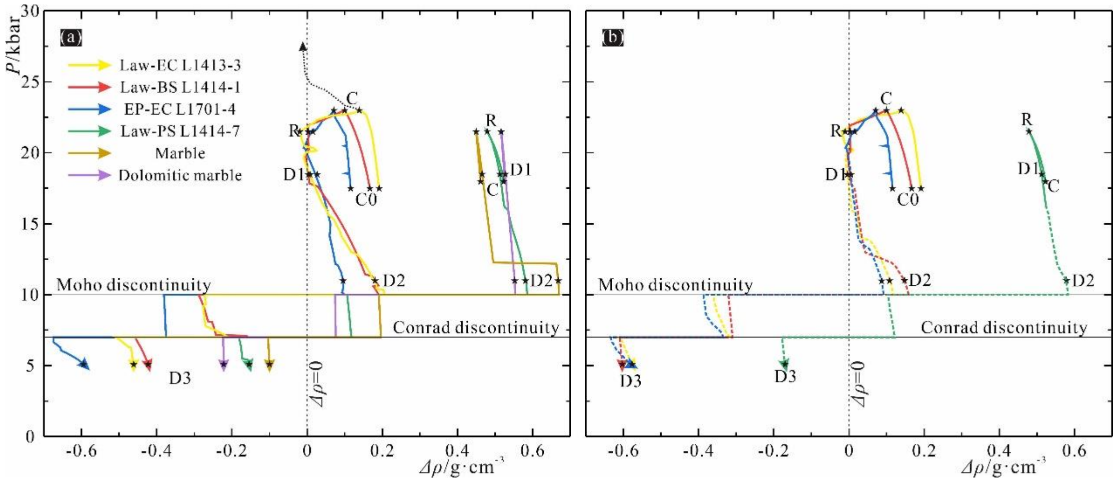


Fig. 10. P-Δρ diagrams of eclogites L1413-3 and L1701-4, lawsonite-bearing blueschist L1414-1 (Wang et al., 2018), lawsonite-bearing phengite schist L1414-7 (Wang et al., 2018) and marbles with bulk compositions of $CaCO_3$ and $CaMg(CO_3)_2$, showing net buoyancy variation along respective P-T-t paths (Fig. 11). (a) $H_2O$ is saturated; (b) $H_2O$ released during metamorphism is 100% lost from rocks. P-T-t path of sample L1414-7 is used for marbles. The black dashed arrow in Fig. 10a refers to Δρ variation of lawsonite-bearing eclogite L1413-3 along the possible

prograde P-T path if subduction continued after $P_{max}$ shown in Fig. 11. Others are the same as Fig. 8.

The density of law-PS sample L1414-7 (Wang et al., 2018) is in the range of 2.594–3.163 g·cm$^{-3}$, which is much lower than those of the eclogites, blueschists and the PREM mantle (Figs. 9d, S1, S3). Its density is mainly governed by pressure, which has a positive correlation. Along the P-T path derived for the law-PS sample L1414-7 (Wang et al., 2018; Fig. 9d), the density increases gently (2.855–2.896 g·cm$^{-3}$) during prograde burial and decreases gradually to ~2.754 g·cm$^{-3}$ during isothermal decompression and cooling decompression (Fig. 9d, S3). As a result, the net buoyancy decreases gently (Δρ=0.522–0.479 g·cm$^{-3}$; Fig. 10) during prograde burial and increases gradually to the maximum of 0.581–0.585 g·cm$^{-3}$ during isothermal decompression. As the decompression P-T path crosses the Moho discontinuity, the net buoyancy decreases sharply to 0.107–0.118 g·cm$^{-3}$. With continual decompression, the net buoyancy changes to negative values of −0.181 to −0.154 g·cm$^{-3}$ as the P-T path crosses the Conrad discontinuity. The density and net buoyancy variations of marbles along their P-T paths resemble those of law-PS sample L1414-7 (Figs. S3 and 10).

Assuming that fluid generated by dehydration reactions is lost from rocks during metamorphism (Guiraud et al., 2001) and that no fluid infiltration occurs, the densities of LT/HP rocks are expected to be considerably higher than the $H_2O$-saturated case (by up to 0.114–0.181 g·cm$^{-3}$; Fig. S3b) along the same isothermal decompression and cooling decompression P-T paths, whereas the buoyancies behave oppositely (Fig. 10b).

## 7. Discussion

### 7.1. Metamorphic P-T evolution of lawsonite-bearing eclogites and blueschists

Based on the petrography, mineral chemistries, and phase equilibria modeling, we confirmed a clockwise P-T path for these newly discovered LT/HP rocks in the Lanling area, and divided the metamorphic process into four stages (Figs. 9 and 11). Namely, (1) pre-peak prograde stage from lawsonite blueschist facies to $P_{max}$ lawsonite eclogite facies, (2) post-$P_{max}$ heating decompression stage from $P_{max}$ lawsonite eclogite facies to $T_{max}$ lawsonite eclogite facies, (3) post-$T_{max}$ isothermal decompression stage from $T_{max}$ lawsonite eclogite facies, through epidote eclogite facies, to epidote amphibolite facies, and (4) late cooling decompression stage from epidote amphibolite facies to greenschist facies. To better constrain the metamorphic evolution of these LT/HP rocks, variations of mineral modes along their P-T paths (Fig. S4) as well as the P-M($H_2O$) pseudosections (Fig. S5) that exhibit the phase relations at the temperature peak conditions are constructed for representative samples.

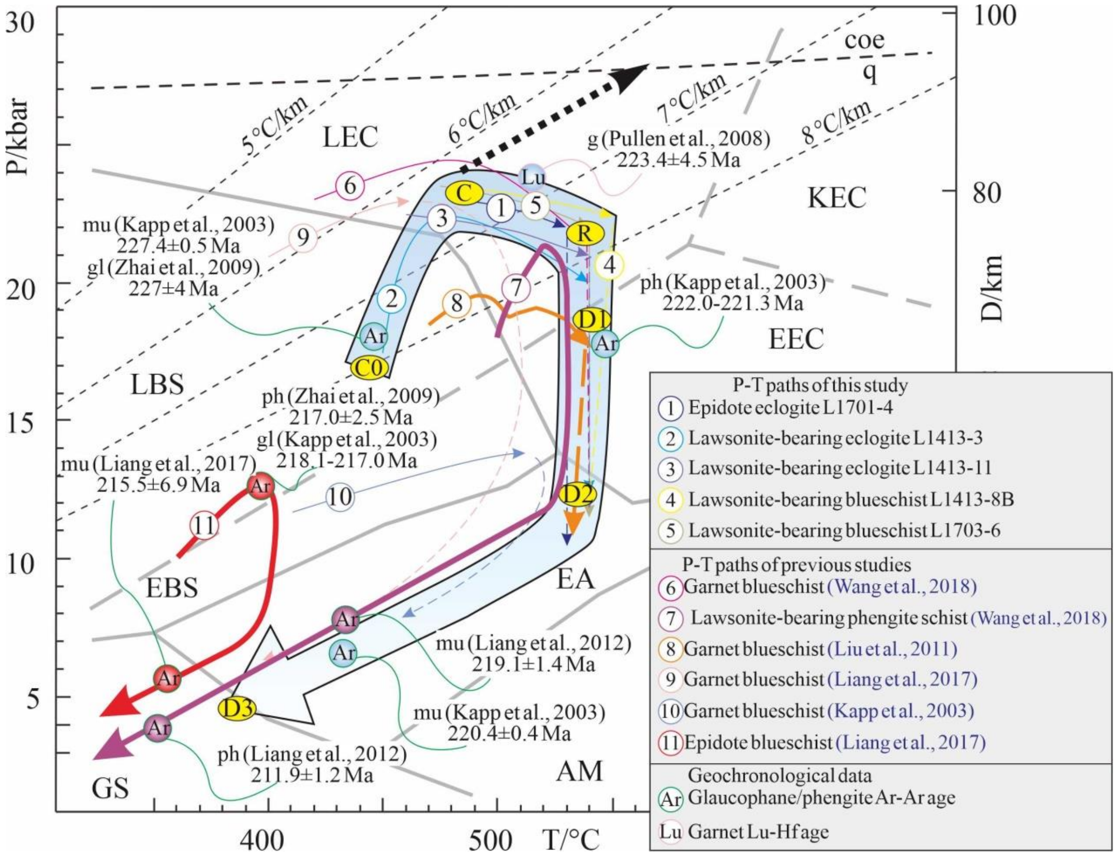


Fig. 11. *P-T*-t paths of the LT/HP metamorphic rocks from the Lanling area, central Qiangtang terrane. The thick translucent, pink and red arrows with geochronological data represent P-T-t paths for eclogites and lawsonite-bearing blueschists, lawsonite-bearing phengite schist and epidote blueschist respectively. The black dashed arrow represents a possible prograde P-T path for eclogites and lawsonite-bearing blueschists if subduction continued after $P_{max}$. Boundaries of metamorphic facies come from Oh and Liou (1998) and Wei et al. (2009a). Geothermal gradients were calculated based on an average density of 3.3 g·cm$^{-3}$. Others the same as Fig. 8.

**Pre-peak prograde metamorphism**

The pre-peak prograde lawsonite blueschist facies metamorphism is suggested to be ~17.5 kbar at ~450 °C (point C0 in Figs. 8d and 11), which is only recorded by the grossular- and spessartine-rich and pyrope-poor inner core of garnet in the Law-EC sample L1413-3 (Fig. 7b). The core of garnet in this sample is inclusion-rich, significantly different from other four samples (Figs. 4–6).

**Post-$P_{max}$ heating decompression**

The $P_{max}$ lawsonite eclogite facies (point C in Figs. 8, 11, and S4) and the $T_{max}$ lawsonite eclogite facies stages (point R in Figs. 8, 11, S4 and S5) are characterized by the core and rim compositions of garnet, respectively; as well as by the primary inclusions in them, i.e., glaucophane, lawsonite/its pseudomorphs, rutile and/or omphacite. In the P-T pseudosections (Figs. 8 and S2), core compositions of garnet in all studied samples reflect lawsonite eclogite facies with $P_{max}$ of 22.5–23.5 kbar at 460–480 °C (a thermal gradient of 6–7 °C·km$^{-3}$; Fig. 11) and predict mineral assemblages of g + o + chl + gl + law ± q ± di for eclogites (samples L1701-4, L1413-3 and L1413-11; Figs. 8a, c and S2a) and g + gl + law ± ta ± act ± chl ± q for blueschists (samples L1413-8B and L1701-6; Figs. 8e and S2c). In contrast, rim compositions of garnet reflect lawsonite eclogite facies with $T_{max}$ of 530–550 °C at 20–22.5 kbar (a thermal gradient of 7–8 °C·km$^{-3}$; Figs. 8, S2 and 11) and predict an assemblage of g + o + gl + law + q for both eclogites and blueschists (Figs. 8b, d, f, S2b and d). The core-to-rim profiles of garnet illustrate a prograde P-T path with heating decompression from $P_{max}$ to $T_{max}$ (Figs. 8, 11 and S2), which is comparable to the data of Liu et al. (2011) and Wang et al. (2018), but differs remarkably from the results of Kapp et al. (2003) and Liang et al. (2017) for garnet blueschists from the same area (Fig. 11). Along the prograde P-T paths (C→R in Figs. 8, 11 and S2), garnet, omphacite and quartz grow at the expense of chlorite, talc, glaucophane and lawsonite. Based on the changes in the mineral modal proportions (Fig. S4), a dehydration reaction is proposed to explain this process:

$$\mathrm{law} + \mathrm{gl} \pm \mathrm{chl} \pm \mathrm{act} \pm \mathrm{ta} = \mathrm{g} + \mathrm{o} + \mathrm{q} + H_2O \quad (1)$$

The $H_2O$ bound in rocks decreases dramatically (by up to 41 % of initial $H_2O$; Fig. S4). These results are in good agreement with the frequent occurrences of glaucophane, lawsonite and its pseudomorphs (box-shaped epidote + paragonite ± chlorite and epidote + albite ± chlorite) in the garnet in each sample (Figs. 4–6). No primary chlorite and talc are recognized in rocks, probably due to their rarity or consumption via the dehydration reaction above (Hernández-Uribe & Palin, 2019).

Our data reveal that although omphacite is not found in the law-BS samples L1413-8B and L1703-6, they both experienced the same peak lawsonite eclogite facies metamorphism as their coexisting eclogites (Fig. 8). Similar conclusions have been drawn from the garnet blueschists in the Lanling area (Liang et al., 2017; Liu et al., 2011; Wang et al., 2018) and the garnet blueschists coexisting with eclogite in the Alpine Corsica (Vitale Brovarone et al., 2011) and the SW Tianshan, China (Tian &

Wei, 2014). Our estimated peak temperature conditions (530–550 °C and 20–22.5 kbar) overlap with those of a garnet blueschist sample L1414-1 (~540 °C and ~21 kbar) and a surrounding law-PS sample L1414-7 (~530 °C and ~21.5 kbar) in the Lanling area (Wang et al., 2018), which were modeled using Theriak-Domino software (de Capitani & Petrakakis, 2010). However, our estimations differ significantly from the results of garnet blueschists based on metamorphic reaction calculation (Kapp et al., 2003; ~520 °C and ~14.3 kbar; Fig. 11), average P-T calculation (Powell et al., 1998; Zhai et al., 2009b; 463–503 °C and 8.3–10 kbar), phase equilibria modeling using Perplex software (Connolly, 2005; Liu et al., 2011; ~535 °C and ~16.8 kbar) and phengite geobarometer and Zr-in-rutile geotherometer ( Liang et al., 2017; Massonne & Schreyer, 1987; Tomkins et al., 2007; ~500 °C and ~21 kbar). These P-T conditions were underestimated, probably due to the fact that lawsonite, instead of chlorite and albite, is ignored as a characteristic component of the peak mineral assemblages.

**Post-$T_{max}$ isothermal decompression**

The post-$T_{max}$ metamorphism is dominated by isothermal decompression, as inferred from the common occurrences of epidote eclogite facies mineral assemblage, epidote + garnet + glaucophane + quartz ± omphacite ± phengite ± paragonite in the matrix, the secondary inclusions of epidote ± paragonite in garnet grains, and the later epidote amphibolite facies overprinting (Figs. 4–6). Along the isothermal decompression P-T path from lawsonite eclogite to epidote eclogite facies (R→D1 in Figs. 8, 11 and S2), a large amount of $H_2O$ in rocks is released as the result of lawsonite decomposition, which originally holds 26–52 % of initial $H_2O$ (R→D1 in Figs. S4 and S5). Based on the changes of the mineral modal proportions (Fig. S4), the dehydration reaction,

$$\mathrm{law} + \mathrm{o} \rightarrow \mathrm{gl} + \mathrm{ep} + \mathrm{g} \pm \mathrm{pa} + \mathrm{H_2O} \qquad (2)$$

is proposed. This reaction results in the consumptions of lawsonite and omphacite and growth of epidote. Fine-grained lawsonite relicts are preserved only as inclusions in the garnet grains from lawsonite-bearing eclogites and blueschists (Figs. 5 and 6). Similarly, little omphacite survived in the matrix of law-EC samples L1413-3 and L1413-11 and law-BS samples L1413-8B and L1701-6 (Figs. 5 and 6). The $H_2O$ released by this reaction further promoted the overgrowth of glaucophane on omphacite in some samples.

The retrograde metamorphism at epidote amphibolite facies (point D2 in Figs. 8, 11 and S2) is characterized by secondary hydrous phases, such as hornblende and epidote, which overprint the eclogite facies minerals (Figs. 4–6). The isothermal decompression P-T path D1→D2 (Figs. 8, 11 and S2) transports high-pressure rocks into the $H_2O$-undersaturated conditions (Fig. S5). If no external $H_2O$ were supplied (e.g., D1→D2 in Fig. S5), the epidote eclogite facies assemblage of ep + g + gl + q + o ± ph ± pa would not be destructed until P <14–16 kbar. In the views that hornblende extensively consumes garnet, omphacite and glaucophane along their cracks or grain boundaries, and omphacite is especially rare or even absent in the lawsonite-bearing rocks, these rocks may have suffered $H_2O$-mediated metasomatism at the epidote amphibolite facies condition. The required $H_2O$ may be supplied by the fluid from lawsonite decomposition in the eclogites and blueschists or from the surrounding hydrous metapelites (Wang et al., 2018) via fluid infiltration (Wei et al., 2010).

**Late cooling decompression**

The late cooling decompression from epidote amphibolite facies to greenschist facies (D2→D3 in Fig. 11) is characterized by the mineral assemblage of actinolite + albite + chlorite, which commonly occurs as coronas around the hornblende, omphacite and garnet grains or as the filling in their cracks (Figs. 4–6).

7.2. P-T-t paths of various LT/HP rocks

**Garnet blueschists**

For garnet blueschists in the core of the Lanling area, a glaucophane $^{40}Ar/^{39}Ar$ plateau age of 227±4 Ma (Zhai et al., 2009b), a garnet Lu-Hf age of 223.4±4.5 Ma (Pullen et al., 2008) and two phengite $^{40}Ar/^{39}Ar$ weight mean plateau ages of 221.4±0.3 Ma and 221.8±0.1 Ma (Kapp et al., 2003) were reported. For the $^{40}Ar/^{39}Ar$ system in glaucophane, a closure temperature of 559 °C can be obtained assuming a cooling rate of 10 $°C \cdot Ma^{-1}$ and a grain size of 0.5 mm (Harrison, 1982). Combined with the fact that the growth of glaucophane commonly initiates at the blueschist facies conditions and that glaucophane tends to decompose accompanied with the growth of garnet and omphacite via reaction (1) during the prograde lawsonite eclogite facies metamorphism (Fig. S5), the glaucophane $^{40}Ar/^{39}Ar$ plateau age of 227±4 Ma most likely represents the timing of glaucophane growth, i.e., an upper limit of the early prograde lawsonite blueschist facies metamorphism.

The $T_{max}$ (530–550 °C) of eclogites and lawsonite-bearing blueschists in the Lanling area are close to the lower limits of Lu-Hf closure temperature in the garnet (>540 °C; Bloch et al., 2015; Scherer et al., 2000). Given that the $Lu^{3+}$ and $Hf^{4+}$ diffusion rates are much lower than those of $Mg^{2+}$ and $Mn^{2+}$(Tirone et al., 2005), the well-preserved growth zoning of garnet with a bell-shaped core-to-rim decrease of spessartine and a gradual increase of pyrope (Fig. 6; Kapp et al., 2003; Liang et al., 2017; Liu et al., 2011; Wang et al., 2018) further indicate that the closure temperature of Lu-Hf in garnet was not overstepped during high-pressure metamorphism (Cheng et al., 2008). Thus, the Lu-Hf age of 223.4±4.5 Ma (Pullen et al., 2008) records garnet growth and can be regarded as a robust timing of the prograde-to-peak lawsonite eclogite facies stages rather than a cooling age.

Phengite is proven to be more retentive in the $^{40}Ar/^{39}Ar$ system than muscovite, as the closure temperatures are up to 600 °C (Forster & Lister, 2014; Lister & Forster, 2016) and down to ~350 °C (McDougall & Harrison, 1999) in phengite and muscovite, respectively. This finding suggests that white mica has great potential to date both the episodic growth and cooling during metamorphism. Using the method of asymptotes and limits (Lister & Forster, 2016), two age spectra of phengite (Kapp et al., 2003) were reinterpreted and three episodes , 227.4±0.5 Ma, 222.0±0.1 to 221.3±0.1 Ma and 220.4±0.4 Ma, were identified (Liang et al., 2017). The first and third episodes correspond to muscovite growth, whereas the second episode shows characteristics of phengite growth (Liang et al., 2017). In the closed systems, the modeled modal proportions of phengite are nearly constant along the proposed P-T paths (Fig. S4). However, due to the high fluid mobility of $K^{+}$ in the open systems, phengite indeed shows episodic growth pulses with distinct occurrences and compositions (Fig. S6), e.g. rarely as inclusions in the garnet (Si=3.00–3.06 pfu; Liang et al., 2017; Liu et al., 2011), but commonly as a component in the garnet-, omphacite- or epidote-bearing veins/aggregates (Si=3.40–3.54 pfu; Fig. 5d; Liang et al., 2017), in the pressure shadows of garnet (Si=3.42–3.44 pfu; Figs. 5a and 6c; Liang et al., 2017), or as coronas (together with chlorite ± albite) around garnet or chloritoid (Si=3.24–3.30 pfu; Liu et al., 2011; Wang et al., 2018). In other words, these three occurrences of phengite may have grown or recrystallized prior to or contemporaneously with garnet growth, after garnet growth and at the greenschist facies conditions respectively. Therefore, the first temporal episode of 227.4±0.5 Ma is a record of the prograde lawsonite blueschist facies stage; the second temporal episode of 222.0±0.1 Ma to 221.3±0.1 Ma may record phengite growth at the epidote eclogite facies stage; the third temporal episode of 220.4±0.4 Ma can be regarded as a lower limit of the greenschist facies stage (Fig. 11).

Combined with the available P-T paths, a P-T-t path with heating decompression is proposed for eclogites and lawsonite-bearing blueschists in the core of the Lanling area (Fig. 11). It reveals that the early prograde metamorphism from lawsonite blueschist to lawsonite eclogite facies may have lasted for <4 Ma, the later prograde metamorphism from lawsonite eclogite to epidote eclogite facies may have sustained for 1.4–2.1 Ma, and the retrograde metamorphism between epidote eclogite facies and greenschist facies may have persisted for >0.9 Ma.

**Garnet-phengite schists**

Two phengite $^{40}Ar/^{39}Ar$ weight mean plateau ages of 219.1±1.4 Ma and 211.9±1.2 Ma were acquired from the garnet-phengite schists in the core of Lanling area (Liang et al., 2012). In the Arrhenius plots, they show characteristics of growth of muscovite and phengite, respectively (Liang et al., 2017). According to discussion above, the age of 219.1±1.4 Ma represents a lower limit of the greenschist facies stage for the garnet-phengite schists, whereas the age of 211.9±1.2 Ma, which is coeval with the intrusion of post-collisional Gangtang Co granitic batholith (209.7–212.5 Ma; Kapp et al., 2003; Li et al., 2015), may record the local heating caused by ductile faulting (Fig. 1; Liang et al., 2012) at upper crust level. Combined with the P-T path acquired by Wang et al. (2018), an incomplete P-T-t path is obtained for the garnet-phengite schists in the core of the Lanling area (Fig. 11).

**Epidote blueschists**

Liang et al. (2017) demonstrates that the epidote blueschists in the mantle region of Lanling area have experienced peak lawsonite blueschist facies metamorphism at ~400 °C and ~11 kbar, subsequent isothermal decompression and final greenschist facies overprinting. Kapp et al., (2003) reported a glaucophane $^{40}Ar/^{39}Ar$ spectrum disturbed by phengite and chlorite, of which steps between 10 and 90 cumulative % $^{39}Ar$ released yield apparent ages of 218.1–210.0 Ma. The maximum apparent ages of 218.1–217.0 Ma might be the least disturbed by phengite and chlorite overgrowth and could be regarded as a record of glaucophane growth during peak lawsonite blueschist facies metamorphism. In addition, phengite $^{40}Ar/^{39}Ar$ spectra with weight mean age of 215±2 Ma (Zhai et al., 2009b), in the Arrhenius plot, displays characteristics of growth of phengite (217.0±2.5 Ma) and muscovite (215.5±6.9 Ma), respectively (Liang et al., 2017). The former may be an upper limit of phengite growth at peak P-T conditions, whereas the latter may be a lower limit of muscovite growth at the greenschist facies stage. The proposed P-T-t path for the epidote blueschists in the mantle of the Lanling area is shown in Fig. 11.

### 7.3. Multi-stage buoyancy-driven exhumation of the LT/HP rocks

Previous studies mainly focused on the role of external tectonic forces, e.g., overthrusting, extrusion and erosion in exhumation of the LT/HP rocks in the CQMB (e.g., Li et al., 2009; Liang et al., 2017; Zhao et al., 2015). However, the effect of internal forces, e.g., buoyancy, on the exhumation of the LT/HP rocks has not been addressed yet. The shape of the P-T-t paths and the late exhumation trait of the Lanling LT/HP rocks (Liang et al., 2017) resemble those of (ultra)high-pressure rocks from other regions in the world, e.g., West Alps (Faryad & Cuthbert, 2020) and New Caledonia (Agard & Vitale Brovarone, 2013; Vitale Brovarone et al., 2018), where (U)HP rocks exhumed with the assistance of subducted low-density buoyant continental crusts following oceanic subduction (Agard et al, 2009). However, this is probably not the case for the CQMB, because there is no convincing evidence for continental subduction coeval with the exhumation of eclogites and blueschists (Zhang et al., 2014).

The P-T-t paths (Fig. 11), and along which the density and net buoyancy variations of the LT/HP rocks in the Lanling area (Figs. 9, 10 and S3), offer us a great opportunity to discuss the role of buoyancy on exhumation of such rocks. A buoyancy-driven exhumation model for LT/HP rocks, is advocated in this study, since it emphasizes the importance of the low-density metasediments in the exhumation process. Three short-lived episodic stages are inferred to interpret the exhumation of lawsonite-bearing eclogites and blueschists.

#### 7.3.1. Principles of exhumation mechanism

There are two major questions: (1) could eclogites and blueschists be able to exhume autonomously by buoyancy along the inferred P-T-t path? and (2) if buoyancy is the dominant driving force for exhumation, will the LT/HP rocks exhume along the subduction channel (e.g., Ernst et al., 1997) or via diapirism (e.g., Little et al., 2011)? To address the above-mentioned questions, we adopted principles from Erdman and

Lee (2014), which can predict or determine the mechanism and the exhumation path of LT/HP rocks, e.g., along subduction channel or via diapirism.

Erdman and Lee (2014) proposed that the fate of (U)HP rocks can be described using a *C*-*D* diagram (Fig. 12) and a parameter *M*, where *C*, *D* and *M* are defined as,

$$C = \frac{V_{\mathrm{C}}}{V_{\mathrm{P}}} = \frac{\Delta\rho g h^2 \sin\alpha}{\eta_{\mathrm{c}} V_{\mathrm{P}}} \qquad (1)$$

$$D = \frac{V_{\mathrm{RT}}}{V_{\mathrm{P}}\sin\alpha} = \frac{\Delta\rho g h^2}{\eta_{\mathrm{m}} V_{\mathrm{P}}\sin\alpha} \qquad (2)$$

$$M = \frac{D}{C} = \frac{V_{\mathrm{C}}\sin\alpha}{V_{\mathrm{RT}}} = \frac{\eta_{\mathrm{c}}}{\eta_{\mathrm{m}}\sin^2\alpha} \qquad (3)$$

where $V_{\mathrm{C}}$, $V_{\mathrm{RT}}$ and $V_{\mathrm{P}}$ are the velocities of the channel flow, the diapiric ascent and the subduction, respectively. *g* is the gravitational acceleration, *h* is the thickness of the subduction channel or the diapir radius, α is the subduction angle, and $\eta_{\mathrm{c}}$ and $\eta_{\mathrm{m}}$ are the viscosities of the subduction channel and surrounding mantle, respectively. If *C*<1 and *D*<1, neither the channel flow nor the diapiric ascent can overcome the downward viscous drag induced by the subducted slab, and the (U)HP rocks tend to subduct. In contrast, if *C*>*D*, i.e., *M*<1, the (U)HP rocks will exhume along the subduction channel; and if *C*<*D*, i.e., *M*>1, the (U)HP rocks will exhume via diapirism.

7.3.2. Parameters for calculations

The parameters invoked in above equations, e.g., the initial thickness *h* of the ascending eclogite and blueschist unit and the subduction angle *α*, are difficult to constrain for ancient subduction zones. Considering that the thickness of the subduction channel and the subduction angle vary in the ranges of 0.3–10 km (Erdman & Lee, 2014; Heuret et al., 2012) and 21–63° (Wada & Wang, 2009), respectively, in the present-today circum-Pacific subduction zones, their average values of *h*=~1.5 km and *α*=~42° are assumed.

The viscosities of the subduction channel and the surround mantle are in the orders of $10^{16}$–$10^{20}$ Pa·s (Shreve & Cloos, 1986) and $10^{18}$–$10^{20}$ Pa·s (Hirth & Kohlstedt, 1996, 2003) respectively; and both of them vary significantly with temperature, volatile content (Erdman & Lee, 2014), and rock types. The LT/HP eclogites and blueschists in the core of Lanling area show $P_{max}$ that is 1.5–2 kbar higher than the surrounding law-PS (sample L1414-7; Fig. 9; Wang et al., 2018), suggesting that the subduction channel lacks metasediments at the depth of return point (corresponding to $P_{max}$). Therefore, a magnitude of $10^{19}$ Pa·s is assumed for $\eta_c$ at the depth of return point. Likewise, the same order of magnitude $10^{19}$ Pa·s is assumed for $\eta_m$, because the surrounding mantle is partial hydrated and weakened by the fluid from LT/HP rocks in the subduction channel. This issue would result in a decrease of $\eta_m$ (Hirth & Kohlstedt, 2003), approaching the value of $\eta_c$.

### 7.3.3. Exhumation mechanisms of Lanling LT/HP rocks at various metamorphic stages

**Initial exhumation (C)**

During burial, the law-EC sample L1413-3 records the prograde metamorphism from lawsonite blueschist facies at ~17.5 kbar, ~450 °C and <227.4–227.0 Ma to $P_{max}$ lawsonite eclogite facies at 22.5–23.5 kbar, 460–480 °C and >~223.4 Ma, indicating an increasing burial depth of ~17 km and a burial rate of >4–5 $mm{\cdot}yr^{-1}$ (Figs. 8, 11 and 13b). The densities of law-EC, ep-EC and law-BS samples (L1413-3, L1701-4, and L1414-1) gradually increase and reach 3.236–3.304 $g{\cdot}cm^{-3}$ at the $P_{max}$ condition (Figs. 9a–c, S3). The positive net buoyancies at the $P_{max}$ ($\Delta\rho$=0.071–0.139 $g{\cdot}cm^{-3}$; Fig. 10a) imply that these LT/HP eclogites and blueschists belong to the self-exhumation type (Chen et al., 2013; Wang et al., 2019). However, if the oceanic crust subducts continuously, e.g. along thick dashed arrow in Fig. 11, the densities of high-pressure rocks will exceed the PREM mantle at 24–25 kbar (i.e., increment of depth by 3–6 km; Figs. 10 and S3), leading to negative net buoyancies and thus potentially resulting in increases of the subduction angle and the subduction rate (Davies & von Blanckenburg, 1995; Ernst et al., 1997), as observed in the convergent margins of the Americas (Klemd et al., 2011 and references therein). As a consequence, at this inflection point, slab will roll back and subsequently break off, once the downward dragging force of slab due to negative net buoyance surpasses the tensile strength of the subducting slab. Integrating with the potential subduction of small continental blocks (Zhang et al., 2014), this scenario would further result in (1) the deceleration and cessation of subduction and initiate subsequent buoyancy-driven exhumation of the top low-density segment from the detached slab, (2) the sinking of the bottom dense segment in the absence of external force, and (3) the upwelling of hot asthenosphere mantle, which may be responsible for the syn-collisional granitic batholith and coeval mafic volcanos in the Qiangtang Terrane (Fig. 13a; Kapp et al., 2003; Li et al., 2015).

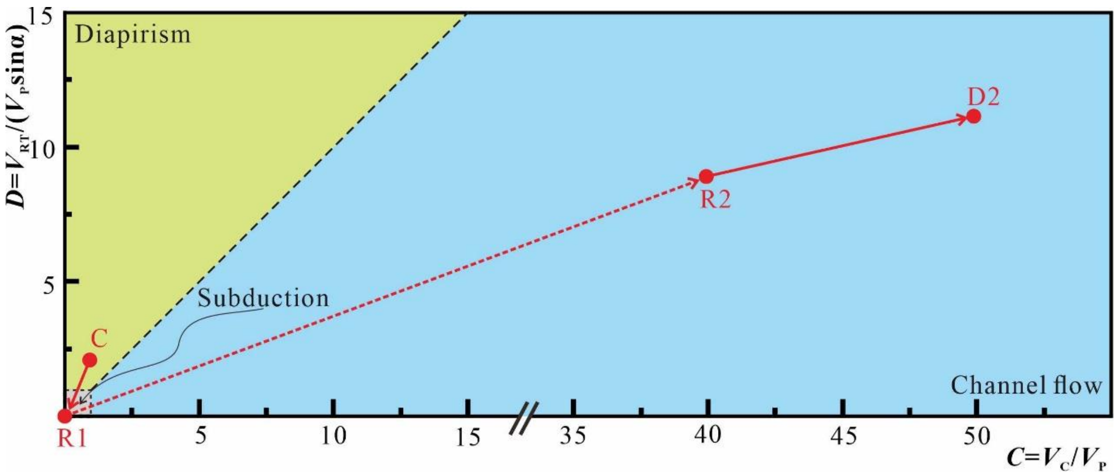

Fig. 12. C-D diagram showing the possible ways of exhumation during heating decompression (C→R1) and isothermal decompression (R2→D2). R1 and R2 refer to before and after eclogites and blueschists were trapped by metasediments at the stage of R in Fig. 9, respectively. Others are the same as Fig. 9.

Taking $\Delta\rho$=0.1 g·cm$^{-3}$, $g$=9.8 m·s$^{-2}$ and $V_P$=5 mm·yr$^{-1}$, the values of parameters $C$, $D$ and $M$ at the initial stage of exhumation are calculated to be ~0.9, ~2.1, and ~2.3 respectively (point C in Fig. 12). These values demonstrate that LT/HP eclogites and blueschists in the core of Lanling area are able to exhume by their own buoyancies and the exhumation path as diapiric rise is favored. This result is consistent with the numerical modeling by Wang et al. (2019), which suggests that without metasediments and serpentinites, subducted oceanic crust tends to exhume via diapirism. The rate of the initial exhumation ($V_E$) can be estimated as,

$$V_E = V_{RT} - V_P \sin a = \frac{\Delta\rho g h^2}{\eta_m} - V_P \sin a. \qquad (4)$$

Taking the same values as above for required parameters, $V_E$ is in the order of mm·yr$^{-1}$. Slab break-off induced eduction (Duretz et al., 2012), subduction reversal (Li et al., 2020; Zhao et al., 2015), or divergence (Liao et al., 2018; Lister & Forster, 2009) for example due to slab-rollback, may also enhance the initial exhumation process.

**Early slow self-exhumation via diapiric rise (heating decompression, C-R1)**

Due to the relatively high densities and low positive net buoyancies (Figs. 9, 10, S3), the initial exhumation of LT/HP eclogites and blueschists in the core of Lanling area (Fig. 13c) probably proceeded at a low rate without the assistance of external driving forces. The slow exhumation via diapiric rise, during which eclogites and blueschists pass through the increasing isotherms (Fig. 13c) and would be heated up by the surrounding mantle and the upwelling hot asthenosphere, produces the heating decompression P-T-t path from the $P_{max}$ at >~223.4 Ma to the $T_{max}$ at >222.0–221.3 Ma with an average exhumation rate of 2–3 mm·yr$^{-1}$, comparable with the calculated $V_E$ above (C → R in Figs. 8, 9, 11). During this process, the abrupt increase of densities and decrease of net buoyancies of eclogites and blueschists (Figs. 9, 10, S3), which are caused by dehydration of low-density hydrous minerals (e.g., lawsonite and glaucophane) and formation of dense anhydrous minerals (e.g., garnet and omphacite; Fig. S6), further obstruct the exhumation and reduce the exhumation rate (Wang et al., 2019). Therefore, as the exhumation continues, the self-exhumation of LT/HP eclogites and blueschists via diapiric rise becomes more and more difficult (Fig. 13d). The negative net buoyancies around the $T_{max}$ ($\Delta\rho \leq 0$; Fig. 10a) suggest that carried-exhumation mechanism of the LT/HP eclogites and blueschists is required.

Taking $\Delta\rho=0$, both $C$ and $D$ at the $T_{max}$ stage are zero (point R1 in Fig. 12). This result means that the eclogites and blueschist should be stalled or sink gravitationally again at the depth of ~75 km if there are no external exhumation-driving forces (Erdman & Lee, 2014).

**Post-$T_{max}$ rapid carried-exhumation along subduction channel (isothermal decompression, R2-D2)**

Metasediments have been proposed to play a crucial role in the exhumation of subducted oceanic crust (e.g., Agard et al., 2009; Wang et al., 2019; Wei et al., 2009b). It is worth noting that eclogites and blueschists commonly occur as blocks or lenses in the matrix of metasediments in the CQMB (Fig. 3; Wang et al., 2018; Zhang et al., 2014; Zhao et al., 2015), which is a common phenomenon in other (U)HP terranes (e.g. Agard et al., 2009 and references therein). Although the host law-PS sample L1414-7 is predicted to have experienced a prograde metamorphism (with slightly higher thermal gradient) different from the enclosed law-EC, ep-EC and law-BS (Fig. 11; Wang et al., 2018), they both experienced similar retrograde metamorphism. Especially, the $P_{max}$ condition of the law-PS (~21.5 kbar) is comparable with the P condition at the $T_{max}$ of the law-EC, ep-EC and law-BS (Fig. 11). This result probably indicates that being trapped by the low-density metasediments (e.g., law-PS and/or marbles; Figs. 10 and S3) detached from the upper part of the downgoing slab, a small portion of the eclogites and blueschists were able to exhume continuously after $T_{max}$.

According to the satellite map, the area ratio of LT/HP metabasites and metasediments is ~1:8.6 in the core of Lanling area. When they mixed, the dominant metasediments would control the overall density and viscosity of the exhuming slice, reducing them to ~2.946 g·cm$^{-3}$ (at 21.5 kbar) and ~$10^{18}$ Pa·s (e.g., Shreve & Cloos, 1986), much lower than the surrounding mantle. The large positive net buoyancy ($\Delta\rho$=~0.429 g·cm$^{-3}$ at 21.5 kbar) and the significant decrease of the viscosity of the subduction channel would facilitate, and more importantly, change the path of exhumation. Take the same values as section 7.3.2, except $\Delta\rho$=~0.429 g·cm$^{-3}$ and $\eta_c$=~$10^{18}$ Pa·s, $C$, $D$, and $M$ at this stage are calculated to be ~40, ~9 and ~0.2, respectively, suggesting that the carried-exhumation of LT/HP eclogites and blueschists occurs along the subduction channel rather than diapirism (point R2 in Fig. 12). This result agrees well with that of the numerical modeling, which reveals that the carried-exhumation should operate in the subduction channel (Schliffke et al., 2019; Wang et al., 2019). During this process, the mixture of eclogites, blueschists and metasediments would ascend nearly parallel to the isotherms, and thus produce a nearly isothermal decompression P-T-t path for all LT/HP rocks (R→D2 in Fig. 11).

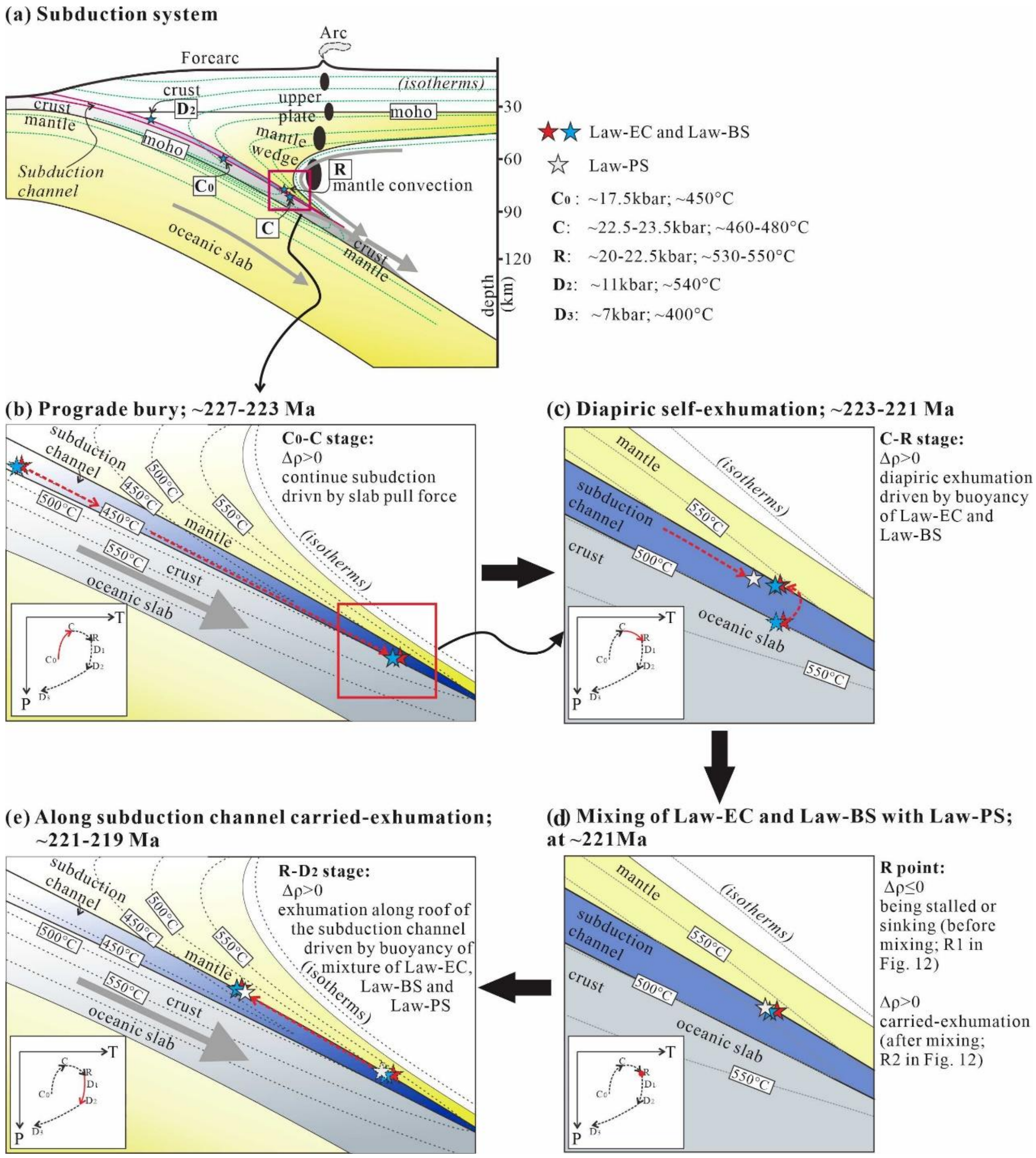


Fig. 13. Tectonic evolution model of the HP/LT metamorphic rocks in the Qiangtang Terrane, central Tibetan Plateau. Details of the evolution process are described in the main text.

Along this isothermal decompression P-T-t path, the densities of both LT/HP metabasites and metasediments decrease significantly and the buoyancies increase, regardless of the bulk $H_2O$ saturation conditions (Figs. 9, 10 and S3). In other words, the mantle-level exhumation of the mixtures of eclogites, blueschists and metasediments from lawsonite eclogite facies (~21.5 kbar or ~75 km at 545 °C) to epidote amphibolite facies (~11 kbar or ~43 km at 540 °C) is greatly eased and the exhumation rate is accelerated. Because the post-$T_{max}$ exhumation with isothermal decompression may have occurred at the period from >222.0–221.3 Ma to >220.4–219.1 Ma, an average exhumation rate of 11–36 mm·$yr^{-1}$ is inferred, which is much faster than the early heating decompression stage. Rapid exhumation rate of similar magnitude has also been reported in natural rocks (DesOrmeau et al., 2018) and numerical modeling (Liao et al., 2018). The rate of exhumation ($V_{\mathrm{E}}$) at this stage can also be estimated by,

$$V_{\mathrm{E}} = (V_{\mathrm{C}} - V_{\mathrm{P}})\sin a = \left(\frac{\Delta\rho g h^2 \sin a}{\eta_{\mathrm{c}}} - V_{\mathrm{P}}\right)\sin a \qquad (5)$$

Taking the same parameter values as those in this section, a $V_{\mathrm{E}}$ in the order of ~$10^2$ mm·yr$^{-1}$ is obtained. However, due to the variations of parameters, e.g., $h$, $a$ and $\eta_{\mathrm{c}}$, and the uncertainty of $\eta_{\mathrm{c}}$ (Erdman & Lee, 2014), this $V_{\mathrm{E}}$ can only be regarded as an approximate value. For example, an increase of $\eta_{\mathrm{c}}$ from $10^{18}$ to $10^{19}$ Pa·s will lead to a decrease of $V_{\mathrm{E}}$ from ~$10^2$ to ~$10^1$ mm·yr$^{-1}$.

**Final slow accretionary wedge-exhumation (cooling decompression, D2-D3)**

As the mixture of LT/HP eclogites, blueschists and metasediments exhumed across the Moho discontinuity and into the lower crustal level (i.e., accretionary wedge), the dramatically decreased net buoyancies for both metabasites (−0.159 to −0.381 g·cm$^{-3}$) and metasediments (0.107–0.118 g·cm$^{-3}$; Fig. 10) result in a significant loss of the carried-exhumation ability and a reduction of exhumation rate. This result may be responsible for the epidote amphibolite facies retrograde metamorphism of eclogites and blueschists at ~11 kbar and ~540 °C (Fig. 11).

As LT/HP rocks exhumed further into the upper crustal level, the negative net buoyancies of metasediments (Fig. 10; e.g., −0.181 to −0.154 g·cm$^{-3}$ for law-PS sample L1414-7) inhibit them to continue to carry eclogites and blueschists upwards. This means that the final exhumation at the crustal level is not assisted by the buoyancy of LT/HP rocks, but more importantly, by the addition of lower density materials and/or the external tectonic forces. The epidote blueschists in the mantle of the Lanling area show isothermal decompression from ~11 kbar to ~7 kbar at ~400 °C, and afterwards, has the same cooling decompression as the LT/HP eclogites and blueschists in the core (Fig. 11; Liang et al., 2017). This phenomenon may imply that the LT/HP rocks in the core of Lanling area were incorporated into the epidote blueschists at the depth of ~30 km.

In the CQMB, the chaotic juxtaposition of eclogite facies, epidote-blueschist facies rocks, sub-greenschist facies, and unmetamorphosed rocks (e.g., Kapp et al., 2003; Zhao et al., 2015) invokes an accretionary wedge model (Platt, 1986; Agard et al., 2009) to account for the final exposure of the LT/HP rocks at the surface during Late Triassic-Early Jurassic. During this accretionary wedge exhumation process, the mixture of LT/HP rocks crosscuts the decreasing isotherms, and thus results in a cooling decompression P-T-t path. Taking into account of the P-T-t paths of all types of LT/HP rocks in the core and mantle, the final exhumation with cooling decompression may occur at the period from >220.4–219.1 Ma to 215.5–211.9 Ma, suggesting an average exhumation rate of 2.5–6 mm·yr$^{-1}$.

Our new data do not agree with the viewpoint that the LT/HP rocks were derived from southward subduction of the Jinsha Paleo-Tethys and later exhumation by domal low angle normal faulting beneath the central Qiangtang Terrane (Kapp et al, 2003). However, more work is needed to identify whether these LT/HP rocks exhumed from northward subduction channel beneath the North Qiangtang Terrane (e.g., Liang et al., 2017) or southward subduction channel beneath the South Qiangtang Terrane (e.g., Zhao et al., 2015).

## 8. Conclusion

1) Lawsonite-bearing eclogites (Law-EC), epidote eclogites (Ep-EC) and lawsonite-bearing blueschists (Law-BS) are discovered for the first time in the core of the Lanling area, Central Qiangtang Terrane, Tibetan Plateau. These LT/HP rocks are characterized by lawsonite or its pseudomorphs (e.g., box-shaped epidote + paragonite ± chlorite and epidote + albite) as inclusions in the garnet. Phase equilibria modeling reveals that both eclogites and blueschists experienced successive early heating decompression from the $P_{max}$ lawsonite eclogite facies at 460–480 °C and 22.5–23.5 kbar to the $T_{max}$ lawsonite eclogite facies at 530–550 °C and 20–22.5 kbar, late isothermal decompression, and final cooling decompression.

2) Combined with previous reported geochronological data, clockwise P-T-t paths are proposed for LT/HP rocks in the Lanling area. These results demonstrate that the subduction of the Paleo-Tethys Ocean commenced at >227.4 Ma, exhumation of eclogites and blueschists in the core of the Lanling area initiated at >223.4 Ma and finalized at <211.9 Ma.

3) Density and net buoyancy calculations reveal multi-staged and buoyancy-driven exhumation process for the LT/HP rocks in the Lanling area: Early slow self-exhumation of eclogites and blueschists via diapiric rise produced the heating

decompression P-T path; post-$T_{max}$ rapid carried-exhumation of eclogites and blueschists assisted by metasediments along subduction channel developed the isothermal decompression P-T path; and final slow accretionary wedge-exhumation of eclogites, blueschists and metasediments in the core and epidote blueschists in the mantle formed the cooling decompression P-T path. These results support the argument that short-lived and discontinuous exhumation is a general rule for the oceanic eclogites and blueschists worldwide (Agard et al., 2009).

## Acknowledgements

We are grateful to Di Xiu, Cui Xu, Shanxia Luo and Zheng changqing for their assistances in the laboratory operation of EMPA and to Huijuan Liu for her XRF analytical work. Dian Li, Chao Li and Benxun Shi are thanked for discussion regarding the regional background. Yilong Zheng is thanked for his assistance in the field work. Yi Zhang, Wenxiang Xu and Hongwei Huang are thanked for their assistances with petrological work. This study is financially supported by the National Natural Science Foundation of China (91755206, 41502059, 41902222). All data used for this paper could be found in the website: https://zenodo.org/record/4451768#.YAfRqDoza70.

## References

Agard, P., & Vitale Brovarone, A. (2013). Thermal regime of continental subduction: The record from exhumed HP-LT terranes (New Caledonia, Oman, Corsica). *Tectonophysics*, 601, 206-215.

Agard, P., Yamato, P., Jolivet, L., & Burov, E. (2009). Exhumation of oceanic blueschists and eclogites in subduction zones: timing and mechanisms. *Earth-Science Reviews*, 92(1-2), 53-79.

Ao, A., & Bhowmik, S.K. (2014). Cold subduction of the Neotethys: the metamorphic record from finely banded lawsonite and epidote blueschists and associated metabasalts of the Nagaland Ophiolite Complex, India. *Journal of Metamorphic Geology*, 32(8), 829-860.

Aoki, I., & Takahashi, E. (2004). Density of MORB eclogite in the upper mantle. *Physics of the Earth and Planetary Interiors*, 143-144, 129-143.

Baldwin, J.A., Powell, R., Brown, M., Moraes, R., & Fuck, R.A. (2005). Modelling of mineral equilibria in ultrahigh-temperature metamorphic rocks from the Anápolis-Itauçu Complex, central Brazil. *Journal of Metamorphic Geology*, 23(7), 511-531.

Bloch, E., Ganguly, J., Hervig, R.L., & Cheng, W.J. (2015). $^{176}$Lu-$^{176}$Hf geochronology of garnet I: experimental determination of the diffusion kinetics of $Lu^{3+}$ and $Hf^{4+}$ in garnet, closure temperatures and geochronological implications. *Contributions to Mineralogy and Petrology*, 169(2), 12.

Carson, C.J., Powell, R., & Clarek, G.L. (1999). Calculated mineral equilibria for eclogites in $CaO$-$Na_2O$-$FeO$-$MgO$-$Al_2O_3$-$SiO_2$-$H_2O$: application to the Pouébo Terrane, Pam Peninsula, New Caledonia. *Journal of Metamorphic Geology*, 17(1), 9-24.

Chen, Y., Ye K., Wu T.F., & Guo S. (2013). Exhumation of oceanic eclogites: thermodynamic constraints on pressure, temperature, bulk composition and density. *Journal of Metamorphic Geology*, 31(5), 549-570.

Cheng, H., King, R.L., Nakamura, E., Vervoort, J.D., & Zhou, Z. (2008). Coupled Lu-Hf and Sm-Nd geochronology constrains garnet growth in ultra-high-pressure eclogites from the Dabie orogen. *Journal of Metamorphic Geology*, 26(7), 741-758.

Chopin, C. (1984). Coesite and pure pyrope in high-grade blueschists of the Western Alps: a first record and some consequences. *Contributions to Mineralogy and Petrology*, 86(2), 107-118.

Coggon, R., & Holland, T.J.B. (2002). Mixing properties of phengitic micas and revised garnet-phengite thermobarometers. *Journal of Metamorphic Geology*, 20(7), 683-696.

Connolly, J.A.D. (2005). Computation of phase equilibria by linear programming: a tool for geodynamic modeling and its application to subduction zone decarbonation. *Earth and Planetary Science Letters*, 236(1-2), 524-541.

Dale, J., Powell, R., White, R.W., Elmer, F.L., & Holland, T.J.B. (2005). A thermodynamic model for Ca-Na clinoamphiboles in $Na_2O$-$CaO$-$FeO$-$MgO$-$Al_2O_3$-$SiO_2$-$H_2O$-$O$ for petrological calculations. *Journal of Metamorphic Geology*, 23(8), 771-791.

Davies, J.H., & von Blanckenburg, F. (1995). Slab breakoff: a model of lithosphere detachment and its test in the magmatism and deformation of collisional orogens. *Earth and Planetary Science Letters*, 129(1), 85-102.

de Capitani, C., & Petrakakis, K. (2010). The computation of equilibrium assemblage diagrams with Theriak/Domino software. *American Mineralogist*, 95(7), 1006-1016.

DesOrmeau, J.W., Gordon, S.M., Little, T.A., Bowring, S.A., Schoene, B., Samperton, K.M., & Kylander-Clark, A.R.C. (2018). Using eclogite retrogression to track the rapid exhumation of the Pliocene Papua New Guinea UHP Terrane. *Journal of Petrology*, 59(10), 2017-2042.

Diener, J.F.A., Powell, R., White, R.W., & Holland, T.J.B. (2007). A new thermodynamic model for clino- and orthoamphiboles in the system $Na_2O$-$CaO$-$FeO$-$MgO$-$Al_2O_3$-$SiO_2$-$H_2O$-$O$. *Journal of Metamorphic Geology*, 25(6), 631-656.

Du, J.X., Zhang, L.F., Bader, T., Chen, Z.Y., & Lü, Z. (2014c). Metamorphic evolution of relict lawsonite-bearing eclogites from the (U)HP metamorphic belt in the Chinese southwestern Tianshan. *Journal of Metamorphic Geology*, 32(6), 575-598.

Du, J.X., Zhang, L.F., Bader, T., & Shen, T.T. (2014b). Metamorphic evolution of ultrahigh-pressure rocks from Chinese southwestern Tianshan and a possible indicator of UHP metamorphism using garnet composition in low-T eclogites. *Journal of Asian Earth Sciences*, 91(SI), 69-88.

Du, J.X., Zhang, L.F., Lü, Z., & Chu, X. (2011). Lawsonite-bearing chloritoid-glaucophane schist from SW Tianshan, China: Phase equilibria and P-T path. *Journal of Asian Earth Sciences*, 42(4SI), 684-693.

Du, J.X., Zhang, L.F., Shen, X.J., & Bader, T. (2014a). A new P-T-t path of eclogites from Chinese southwestern Tianshan: constraints from P-T pseudosections and Sm-Nd isochron dating. *Lithos*, 200-201, 258-272.

Duretz, T., Gerya, T.V., Kaus, B.J.P., & Andersen, T.B. (2012). Thermomechanical modeling of slab eduction. *Journal of Geophysical Research: Solid Earth*, 117, B08411.

Dziewonski, A.M., & Anderson, D.L. (1981). Preliminary reference Earth model. *Physics of the Earth and Planetary Interiors*, 25(4), 297-356.

Erdman, M.E., & Lee, C.A. (2014). Oceanic- and continental-type metamorphic terranes: occurrence and exhumation mechanisms. *Earth-Science Reviews*, 139, 33-46.

Ernst, W.G. (2001). Subduction, ultrahigh-pressure metamorphism, and regurgitation of buoyant crustal slices — implications for arcs and continental growth. *Physics of the Earth and Planetary Interiors*, 127(1), 253-275.

Ernst, W.G., Maruyama, S., & Wallis, S. (1997). Buoyancy-driven, rapid exhumation of ultrahigh-pressure metamorphosed continental crust. *Proceedings of the National Academy of Sciences*, 94(18), 9532-9537.

Faryad, S.W., & Cuthbert, S.J. (2020). High-temperature overprint in (U)HPM rocks exhumed from subduction zones; A product of isothermal decompression or a consequence of slab break-off (slab rollback)? *Earth-Science Reviews*, 202, 103108.

Forster, M.A., & Lister, G.S. (2014). $^{40}Ar/^{39}Ar$ geochronology and the diffusion of $^{39}Ar$ in phengite-muscovite intergrowths during step-heating experiments in vacuo. In: Jourdan, F., Mark, D.F., & Verati, C. (Eds.), Advances in $^{40}Ar/^{39}Ar$ dating: from archaeology to planetary sciences. Geological Society, London, Special Publications, 378(1), 117-135.

Green, E., Holland, T., & Powell, R. (2007). An order-disorder model for omphacitic pyroxenes in the system jadeite-diopside-hedenbergite-acmite, with applications to eclogitic rocks. *American Mineralogist*, 92(7), 1181-1189.

Guiraud, M., Powell, R., & Rebay, G. (2001). $H_2O$ in metamorphism and unexpected behaviour in the preservation of metamorphic mineral assemblages. *Journal of Metamorphic Geology*, 19(4), 445-454.

Hacker, B. R., Gerya, T. V., & Gilotti, J. A. (2013). Formation and exhumation of ultrahigh-pressure terranes. *Elements*, 9(4), 289-293.

Harrison, T.M. (1982). Diffusion of $^{40}Ar$ in Hornblende. *Contributions to Mineralogy and Petrology*, 78(3), 324-331.

Hermann, J., Müntener, O., & Scambelluri, M. (2000). The importance of serpentinite mylonites for subduction and exhumation of oceanic crust. *Tectonophysics*, 327 (3-4), 225-238.

Hernández-Uribe, D., & Palin, R.M. (2019). A revised petrological model for subducted oceanic crust: insights from phase equilibrium modelling. *Journal of Metamorphic Geology*, 37(6), 745-768.

Heuret, A., Conrad, C.P., Funiciello, F., Lallemand, S., & Sandri, L. (2012). Relation between subduction megathrust earthquakes, trench sediment thickness and upper plate strain. *Geophysical Research Letters*, 39, L05304.

Hirth, G., Kohlstedt, D.L. (1996). Water in the oceanic upper mantle: implications for rheology, melt extraction and the evolution of the lithosphere. *Earth and Planetary Science Letters*, 144(1-2), 93-108.

Hirth, G., Kohlstedt, D.L. (2003). Rheology of the upper mantle and the mantle wedge: a view from the experimentalists. In: Eiler, J. (Eds.), Inside the Subduction Factory. Geophysical Monograph American Geophysical Union, Washington, D.C., 83-105.

Holland, T.J.B., & Powell, R. (1998). An internally consistent thermodynamic data set for phases of petrological interest. *Journal of Metamorphic Geology*, 16(3), 309-343.

Holland, T., & Powell, R. (2003). Activity-composition relations for phases in petrological calculations: an asymmetric multicomponent formulation. *Contributions to Mineralogy and Petrology*, 145(4), 492-501.

Hu, P.Y., Zhai, Q.G., Jahn, B.M., Wang, J., Li, C., Lee, H.Y, & Tang, S.H. (2015). Early Ordovician granites from the South Qiangtang terrane, northern Tibet: implications for the early Paleozoic tectonic evolution along the Gondwanan proto-Tethyan margin. *Lithos*, 220-223, 318-338.

Irifune, T., Sekine, T., Ringwood, A.E., & Hibberson, W.O. (1986). The eclogite-garnetite transformation at high pressure and some geophysical implications. *Earth and Planetary Science Letters*, 77(2), 245-256.

Jiang, Q.Y., Li, C., Su, L., Hu, P.Y., Xie, C.M., & Wu, H. (2015). Carboniferous arc magmatism in the Qiangtang area, northern Tibet: Zircon U-Pb ages, geochemical and Lu-Hf isotopic characteristics, and tectonic implications. *Journal of Asian Earth Sciences*, 100, 132-144.

Kapp, P., & Decelles, P.G. (2019). Mesozoic-Cenozoic geological evolution of the Himalayan-Tibetan orogen and working tectonic hypotheses. *American Journal of Science*, 319(3), 159-254.

Kapp, P., Yin, A., Manning, C.E., Harrison, T.M., Taylor, M.H., & Ding, L. (2003). Tectonic evolution of the early Mesozoic blueschist-bearing Qiangtang metamorphic belt, central Tibet. *Tectonics*, 22(4), 1043.

Kapp, P., Yin, A., Manning, C.E., Murphy, M., Harrison, T.M., Spurlin, M., Ding, L., Deng, X.G., & Wu, C.M. (2000). Blueschist-bearing metamorphic core complexes in the Qiangtang block reveal deep crustal structure of northern Tibet. *Geology*, 28(1), 19-22.

Klemd, R., John, T., Scherer, E.E., Rondenay, S., & Gao, J. (2011). Changes in dip of subducted slabs at depth: petrological and geochronological evidence from HP-UHP rocks (Tianshan, NW-China). *Earth and Planetary Science Letters*, 310(1-2), 9-20.

Leake, B.E., Woolley, A.R., Arps, C.E.S., Birch, W.D., Gilbert, M.C., Grice, J.D., Hawthorne, F.C., Kato, A., Kisch, H.J., Krivovichev, V.G., Linthout, K., Laird, J., Mandarino, J.A., Maresch, W.V., Nickel, E.H., Rock, N.M.S., Schumacher, J.C., Smith, D.C., Stephenson, N.C.N., Ungaretti, L., Whittaker, E.J.W., & Guo, Y.Z. (1997). Nomenclature of amphiboles: report of the subcommittee on amphiboles of the international mineralogical association, commission on new minerals and mineral names. *The Canadian Mineralogist*, 35, 219-246.

Li, C., Zhai, Q.G., Dong, Y.S., & Huang, X.P. (2006). Discovery of eclogite and its geological significance in Qiangtang area, central Tibet. *Chinese Science Bulletin*, 51(9), 1095-1100.

Li, C., Zhai, Q.G., Dong, Y.S., Liu, S., Xie, C.M., & Wu, Y.W. (2009). High-pressure eclogite-blueschist metamorphic belt and closure of paleo-Tethys Ocean in Central Qiangtang, Qinghai-Tibet plateau. *Journal of Earth Science*, 20(2), 209-218.

Li, D., Wang, G.H., Bons, P.D., Zhao, Z.B., Du, J.X., Wang, S.L., Yuan, G.L., Liang, X., Zhang, L., Li, C., Fang, D.R., Tang, Y., Hu, Y.L., & Fu, Y.Z. (2020). Subduction reversal in a divergent double subduction zone drives the exhumation of southern Qiangtang blueschist-bearing mélange, central Tibet. *Tectonics*, 39(4), e2019TC006051.

Li, D., Wang, G.H., Gao, J.H., Yuan, G.L., Zhou, J., Fang, D.R., Zhang, L., Gong, Y.D., & Zhao, H.C. (2018). The continental subduction in the evolution of central qiangtang mélange belt and its tectonic significance. *International Geology Review*, 61(9), 1143-1170.

Li, G.M., Li, J.X., Zhao, J.X., Qin, K.Z., Cao, M.J., & Evans, N.J. (2015). Petrogenesis and tectonic setting of Triassic granitoids in the Qiangtang terrane, central Tibet: evidence from U-Pb ages, petrochemistry and Sr-Nd-Hf isotopes. *Journal of Asian Earth Sciences*, 105, 443-455.

Liang, X., Wang, G.H., Yang, B., Ran, H., Zheng, Y.L., Du, J.X., & Li, L.G. (2017). Stepwise exhumation of the Triassic Lanling high-pressure metamorphic belt in Central Qiangtang, Tibet: insights from a coupled study of metamorphism, deformation, and geochronology. *Tectonics*, 36(4), 652-670.

Liang, X., Wang, G.H., Yuan, G.L., & Liu, Y. (2012). Structural sequence and geochronology of the Qomo Ri accretionary complex, central Qiangtang, Tibet: implications for the late Triassic subduction of the Paleo-Tethys Ocean. *Gondwana Research*, 22(2), 470-481.

Liao, J., Malusà, M.G., Zhao, L., Baldwin, S.L., Fitzgerald, P.G., & Gerya, T. (2018). Divergent plate motion drives rapid exhumation of (ultra)high pressure rocks. *Earth and Planetary Science Letters*, 491, 67-80.

Lister, G.S., & Forster, M.A. (2009). Tectonic mode switches and the nature of orogenesis. *Lithos*, 113(1-2), 274-291.

Lister, G.S., & Forster, M.A. (2016). White mica $^{40}Ar/^{39}Ar$ age spectra and the timing of multiple episodes of high-P metamorphic mineral growth in the Cycladic eclogite-blueschist belt, Syros, Aegean Sea, Greece. *Journal of Metamorphic Geology*, 34(5), 401-421.

Little, T.A., Hacker, B.R., Gordon, S.M., Baldwin, S.L., Fitzgerald, P.G., Ellis, S., & Korchinski,

M. (2011). Diapiric exhumation of Earth's youngest (UHP) eclogites in the gneiss domes of the D'Entrecasteaux Islands, Papua New Guinea. *Tectonophysics*, 510(1-2), 39-68.

Liu, Y., Santosh, M., Zhao, Z.B., Niu, W.C., & Wang, G.H. (2011). Evidence for palaeo-Tethyan oceanic subduction within central Qiangtang, northern Tibet. *Lithos*, 127(1-2), 39-53.

Lu, J.P., Zhang, N., Huang, W.H., Tang, Z.H., Li, Y.K., Xu, H., Zhou, Q.E., Lu, G., & Li, Q. (2006). Characteristics and significance of the metamorphic minerals glaucophane-lawsonite assemblage in the Hongjishan area, north-central Qiangtang, northern Tibet, China. *Geological Bulletin of China*, 25(1-2), 70-75. (in Chinese with English abstract)

Marmo, B.A., Clarke, G.L., & Powell, R. (2002). Fractionation of bulk rock composition due to porphyroblast growth: effects on eclogite facies mineral equilibria, Pam Peninsula, New Caledonia. *Journal of Metamorphic Geology*, 20(1), 151-165.

Massonne, H.J., & Schreyer, W. (1987). Phengite geobarometry based on the limiting assemblage with K-feldspar, phlogopite, and quartz. *Contributions to Mineralogy and Petrology*, 96(2), 212-224.

McDougall, I., & Harrison, T.M. (1999). Geochronology and thermochronology by the $^{40}$Ar/$^{39}$Ar Method. Oxford University Press, New York, 269.

Morimoto, N., Fabries, J., Ferguson, A.K., Ginzburg, I.V., Ross, M., Seifert, F.A., Zussman, J., Aoki, K., & Gottardi, G. (1988). Nomenclature of Pyroxenes. *American Mineralogist*, 73(9-10), 1123-1133.

Oh, C.W., & Liou, J.G. (1998). A petrogenetic grid for eclogite and related facies under high-pressure metamorphism. *The Island Arc*, 7(1-2), 36-51.

Platt, J. P. (1986). Dynamics of orogenic wedges and the uplift of high-pressure metamorphic rocks. *Geological Society of America Bulletin*, 97(9), 1037-1053.

Platt, J. P. (1993). Exhumation of high-pressure rocks: a review of concepts and processes. *Terra Nova*, 5(2), 119-133.

Powell, R., Holland, T., & Wroley, B. (1998). Calculating phase diagrams involving solid solutions via non-linear equations, with examples using THERMOCALC. *Journal of Metamorphic Geology*, 16(4), 577-588.

Pullen, A., & Kapp, P. (2014). Mesozoic tectonic history and lithospheric structure of the Qiangtang terrane: insights from the Qiangtang metamorphic belt, central Tibet. In: Nie, J., Horton, B.K., & Hoke, G.D. (Eds.), Toward an improved understanding of uplift mechanisms and the elevation history of the Tibetan Plateau. Geological Society of America Special Paper, 507.

Pullen, A., Kapp, P., Gehrels, G.E., Vervoort, J.D., & Ding, L. (2008). Triassic continental subduction in central Tibet and Mediterranean-style closure of the Paleo-Tethys Ocean. *Geology*, 36(5), 351-354.

Reuber, G., Kaus, B. J. P., Schmalholz, S. M., & White, R. W. (2016). Nonlithostatic pressure during subduction and collision and the formation of (ultra)high-pressure rocks. *Geology*, 44(5), 343-346.

Ricolleau, A., Perrillat, J., Fiquet, G., Daniel, I., Matas, J., Addad, A., Menguy, N., Cardon, H., Mezouar, M., & Guignot, N. (2010). Phase relations and equation of state of a natural MORB: implications for the density profile of subducted oceanic crust in the Earth's lower mantle. *Journal of Geophysical Research*, 115, B08202.

Scherer, E.E., Cameron, K.L., & Blichert-Toft, J. (2000). Lu-Hf garnet geochronology: closure temperature relative to the Sm-Nd system and the effects of trace mineral inclusions. *Geochimica et Cosmochimica Acta*, 64(19), 3413-3432.

Schliffke, N., van Hunen, J., Magni, V., & Allen, M.B. (2019). The role of crustal buoyancy in the generation and emplacement of magmatism during continental collision. *Geochemistry, Geophysics, Geosystems*, 20(11), 4693-4709.

Scodina, M., Cruciani, G., Franceschelli, M., & Massonne, H.J. (2019). Anticlockwise P-T evolution of amphibolites from NE Sardinia, Italy: geodynamic implications for the tectonic evolution of the Variscan Corsica-Sardinia block. *Lithos*, 324-325, 763-775.

Shreve, R.L., & Cloos, M. (1986). Dynamics of sediment subduction, melange formation, and prism accretion. *Journal of Geophysical Research*, 91(B10), 10229-10245.

Sobolev, N. V., & Shatsky, V. S. (1990). Diamond inclusions in garnets from metamorphic rocks: a new environment for diamond formation. *Nature*, 343(6260), 742-746.

Spear, F.S. (1993). Metamorphic phase equilibria and pressure-temperature-time paths. Mineralogical Society of America, Washington, DC, 799 pp.

Tang, X.C., & Zhang, K.J. (2014). Lawsonite- and glaucophane-bearing blueschists from NW Qiangtang, northern Tibet, China: mineralogy, geochemistry, geochronology, and tectonic implications. *International Geology Review*, 56(2), 150-166.

Tian, Z.L., & Wei, C.J. (2014). Coexistence of garnet blueschist and eclogite in South Tianshan, NW China: dependence of P-T evolution and bulk-rock composition. *Journal of Metamorphic Geology*, 32(7), 743-764.

Tirone, M., Ganguly, J., Dohmen, R., Langenhorst, F., Hervig, R., & Becker, H.W. (2005). Rare earth diffusion kinetics in garnet: experimental studies and applications. *Geochimica et Cosmochimica Acta*, 69(9), 2385-2398.

Tomkins, H.S., Powell, R., & Ellis, D.J. (2007). The pressure dependence of the zirconium-in-rutile thermometer. *Journal of Metamorphic Geology*, 25(6), 703-713.

Vitale Brovarone, A., Agard, P., Monié, P., Chauvet, A., & Rabaute, A. (2018). Tectonic and metamorphic architecture of the HP belt of New Caledonia. *Earth-Science Reviews*, 178, 48-67.

Vitale Brovarone, A., Groppo, C., Hetényi, G., Compagnoni, R., & Malavieille, J. (2011). Coexistence of lawsonite-bearing eclogite and blueschist: phase equilibria modelling of Alpine Corsica metabasalts and petrological evolution of subducting slabs. *Journal of Metamorphic Geology*, 29(5), 583-600.

Wada, I., Wang, K.L. (2009). Common depth of slab-mantle decoupling: reconciling diversity and uniformity of subduction zones. *Geochemistry, Geophysics, Geosystems*, 10(10), Q10009.

Wang, S.L., Du, J.X., Wang, G.H., & Liang, X. (2018). Metamorphic P-T paths of blueschist and lawsonite-bearing phengite schist in Lanling area, central Qiangtang. *Earth Science*, 43(4), 1237-1252. (in Chinese with English abstract)

Wang, Y., Zhang, L.F., Li, Z.H., Li, Q.Y., & Bader, T. (2019). The exhumation of subducted oceanic-derived eclogites: insights from phase equilibrium and thermomechanical modeling. *Tectonics*, 38(5), 1764-1797.

Warren, C. J. (2013). Exhumation of (ultra-)high-pressure terranes: concepts and mechanisms. *Solid Earth*, 4(1), 75-92.

Warren, C. J., Beaumont, C., & Jamieson, R.A. (2008). Modelling tectonic styles and ultra-high pressure (UHP) rock exhumation during the transition from oceanic subduction to continental collision. *Earth and Planetary Science Letters*, 267(1-2), 129-145.

Wei, C.J., & Clarke, G.L. (2011). Calculated phase equilibria for MORB compositions: a reappraisal of the metamorphic evolution of lawsonite eclogite. *Journal of Metamorphic Geology*, 29(9), 939-952.

Wei, C.J., Li, Y.J., Yu, Y., & Zhang, J.S. (2010). Phase equilibria and metamorphic evolution of glaucophane-bearing UHP eclogites from the Western Dabieshan Terrane, Central China. *Journal of Metamorphic Geology*, 28(6), 647-666.

Wei, C.J., Wang, W., Clarke, G.L., Zhang, L.F., & Song, S.G. (2009b). Metamorphism of high/ultrahigh-pressure pelitic-felsic schist in the South Tianshan orogen, NW China: phase equilibira and P-T path. *Journal of Petrology*, 50(10), 1973-1991.

Wei, C.J., Yang, Y., Su, X.L., Song, S.G., & Zhang, L.F. (2009a). Metamorphic evolution of low-T eclogite from the North Qilian orogen, NW China: evidence from petrology and calculated phase equilibria in the system NCKFMASHO. *Journal of Metamorphic Geology*, 27(1), 55-70.

White, R.W., Pomroy, N.E., & Powell, R. (2005). An in situ metatexite-diatexite transition in upper amphibolite facies rocks from Broken Hill, Australia. *Journal of Metamorphic Geology*, 23(7), 579-602.

Whitney, D.L., Fornash, K.F., Kang, P., Ghent, E.D., Martin, L., Okay, A.I., & Vitale Brovarone, A. (2020). Lawsonite compostion and zoning as tracers of subduction processes: a global review. *Lithos*, 370-371, 105636.

Yamato, P., & Brun, J. P. (2017). Metamorphic record of catastrophic pressure drops in subduction zones. *Nature Geoscience*, 10(1), 46-50.

Yin, A., & Harrison, T.M. (2000). Geologic evolution of the Himalayan-Tibetan orogen. *Annual Review of Earth and Planetary Sciences*, 28, 211-280.

Zhai, Q.G., Jahn, B., Zhang, R.Y., Wang, J., & Su, L. (2011b). Triassic subduction of the Paleo-Tethys in northern Tibet, China: evidence from the geochemical and isotopic characteristics of eclogites and blueschists of the Qiangtang Block. *Journal of Asian Earth Sciences*, 42(6), 1356-1370.

Zhai, Q.G., Wang, J., Chen, W., & Zhang, Y. (2009b). Petrology, mineralogy and $^{40}Ar/^{39}Ar$ chronology for Rongma blueschist from central Qiangtang, northern Tibet. *Acta Petrologica Sinica*, 25(9), 2281-2288. (in Chinese with English abstract)

Zhai, Q.G., Wang, J., & Wang, Y. (2009a). Discovery of eclogite at Gangmacuo area from Gerze County, Tibet, China. *Geological Bulletin of China*, 28(12), 1720-1724. (in Chinese with English abstract)

Zhai, Q.G., Zhang, R.Y., Jahn, B., Li, C., Song, S.G., & Wang, J. (2011a). Triassic eclogites from central Qiangtang, northern Tibet, China: Petrology, geochronology and metamorphic P-T path. *Lithos*, 125(1-2), 173-189.

Zhang, K.J., Cai, J.X., Zhang, Y.X., & Zhao, T.P. (2006a). Eclogites from central Qiangtang, northern Tibet (China) and tectonic implications. *Earth and Planetary Science Letters*, 245(3-4), 722-729.

Zhang, X.Z., Dong, Y.S., Li, C., Shi, J.R., & Wang, S.Y. (2010). Geochemistry and tectonic significance of eclogites in central Qiangtang, Tibetan Plateau. *Geological Bulletin of China*, 29(12), 1804-1814. (in Chinese with English abstract)

Zhang, X.Z., Dong, Y.S., Li, C., Xie, C.M., Wang, M., Deng, M.R., & Zhang, L. (2014). A record of complex histories from oceanic lithosphere subduction to continental subduction and collision: constraints on geochemistry of eclogite and blueschist in central Qiangtang, Tibetan Plateau. *Acta Petrologica Sinica*, 30(10), 2821-2834. (in Chinese with English abstract)

Zhang, K.J., Zhang, Y.X., Li, B., Zhu, Y.T., & Wei, R.Z. (2006b). The blueschist-bearing Qiangtang metamorphic belt (northern Tibet, China) as an in situ suture zone: evidence from geochemical comparison with the Jinsa suture. *Geology*, 34(6), 493-496.

Zhao, Z.B., Bons, P.D., Wang, G.H., Liu, Y., & Zheng, Y. (2014). Origin and pre-Cenozoic evolution of the south Qiangtang basement, Central Tibet. *Tectonophysics*, 623, 52-66.

Zhao, Z.B., Bons, P.D., Wang, G.H., Soesoo, A., & Liu, Y. (2015). Tectonic evolution and high-pressure rock exhumation in the Qiangtang terrane, central Tibet. *Solid Earth*, 6(2), 457-473.